Monthly Notices of the ROYAL ASTRONOMICAL SOCIETY

MNRAS **446,** 2186–2204 (2015) doi:10.1093/mnras/stu2224

# IFU observations of luminous type II AGN – I. Evidence for ubiquitous winds

Rebecca McElroy,[1,2]★ Scott M. Croom,[1,2] Michael Pracy,[1] Rob Sharp,[2,3] I-Ting Ho[4] and Anne M. Medling[3]

[1]*Sydney Institute for Astronomy, School of Physics, University of Sydney, NSW 2006, Australia*
[2]*ARC Centre of Excellence for All-sky Astrophysics (CAASTRO)*
[3]*Research School of Astronomy & Astrophysics, The Australian National University, Cotter Road, Weston Creek, ACT 2611, Australia*
[4]*Institute for Astronomy, University of Hawaii, 2680 Woodlawn Drive, Honolulu, HI 96822, USA*

Accepted 2014 October 22. Received 2014 October 21; in original form 2014 August 29

## ABSTRACT

We present observations of 17 luminous ($\log(L_{[\mathrm{O\,III}]}/\mathrm{L}_{\odot}) > 8.7$) local ($z < 0.11$) type II AGN. Our aim is to investigate the prevalence and nature of AGN-driven outflows in these galaxies by combining kinematic and ionization diagnostic information. We use non-parametric methods (e.g. $W_{80}$, the width containing 80 per cent of the line flux) to assess the line widths in the central regions of our targets. The maximum values of $W_{80}$ in each galaxy are in the range 400–1600 km s$^{-1}$, with a mean of 790 ± 90 km s$^{-1}$. Such high velocities are strongly suggestive that these AGN are driving ionized outflows. Multi-Gaussian fitting is used to decompose the velocity structure in our galaxies. 14/17 of our targets require three separate kinematic components in the ionized gas in their central regions. The broadest components of these fits have FWHM = 530–2520 km s$^{-1}$, with a mean value of 920 ± 50 km s$^{-1}$. By simultaneously fitting both the H$\beta$/[O III] and H$\alpha$/[N II] complexes, we construct ionization diagnostic diagrams for each component. 13/17 of our galaxies show a significant (>95 per cent) correlation between the [N II]/H$\alpha$ ratio and the velocity dispersion of the gas. Such a correlation is the natural consequence of a contribution to the ionization from shock excitation and we argue that this demonstrates that the outflows from these AGN are directly impacting the surrounding ISM within the galaxies.

**Key words:** galaxies: active – galaxies: evolution – galaxies: kinematics and dynamics – quasars: emission lines.

## 1 INTRODUCTION

The importance of AGN feedback in galaxy evolution is evident from the observed correlations between the mass of galaxies' supermassive black holes (SMBHs) and their stellar bulges (e.g. Tremaine et al. 2002). This correlation suggests a co-dependence between the evolution of galaxies and their SMBHs, leading to the belief that the same process may limit the further growth of both systems. AGN-driven outflows are often invoked as this mechanism. The growth of SMBHs occurs through accretion during active phases. The stellar bulge grows as gas inside the galaxy collapses to form stars, or through accretion of previous generations of stars via mergers. Outflows can remove the gas required for both processes.

Simulations have shown that feedback processes are necessary to reproduce realistic galaxies (e.g. Hopkins et al. 2006), and observations of massive galaxies require a phenomenon such as radio-mode feedback to explain the steep cut-off in their luminosity function (Bower et al. 2006; Croton et al. 2006), though in this paper we will focus on radiatively efficient quasar-mode feedback. It is believed that this cut-off is due to outflows removing or heating gas in these massive galaxies. This inhibits star formation and further AGN activity leading to a lower galaxy luminosity than otherwise predicted and limits the upper mass the galaxy can attain (e.g. Scannapieco & Oh 2004; Murray, Quataert & Thompson 2005). Outflows likely cause the observed enrichment of the intergalactic medium with metals generated in star formation (e.g. Cowie et al. 1995). This has been shown through analysis of quasar absorption spectra and suggests that at least some of the gas driven by galactic winds can escape galaxies.

The exact role of AGN feedback is not well constrained. It is thought that the majority of AGN hosts possess outflows (Ganguly & Brotherton 2008), but that those in higher luminosity AGN are more powerful (Veilleux et al. 2013). While limited insight into outflows within galaxies may be provided by single spectrum

★E-mail: rmcelroy@physics.usyd.edu.au

© 2014 The Authors
Published by Oxford University Press on behalf of the Royal Astronomical Society

Downloaded from http://mnras.oxfordjournals.org/ at The Australian National University on July 12, 2016

surveys such as SDSS (see Barrows et al. 2013), spatial information is required to fully understand the dynamics at play within these galaxies. Integral field spectroscopy (IFS) is the perfect tool for this as it provides spatially resolved spectra across the 2D projection of galaxies, meaning that conditions in different regions of the galaxy may be explored. Several small integral field unit (IFU) surveys of AGN and starburst galaxies have been successful in identifying outflows. Studies such as Sharp & Bland-Hawthorn (2010) concentrated on very nearby AGN and starburst galaxies known to have galactic winds. From this, they found that starburst winds tend to have shock ionization, and that AGN generally excite AGN-ionized winds. These imply different time-scales as due to a starburst's shorter lifetime, by the time the wind is visible, many of the OB stars will have already gone supernova and the radiation driving the wind will be reduced significantly. We now know that winds are not particularly rare; Ganguly & Brotherton (2008) showed that they are present in at least 60 per cent of AGN in their study of single absorption spectra of quasi-stellar objects (QSOs), and as such broader surveys of previously unstudied objects are being pursued.

In their study of 11 luminous, obscured, radio-quiet quasars from the Reyes et al. (2008) catalogue with an average $z \sim 0.55$, Liu et al. (2013) found that outflows were common using non-parametric measures of line width and asymmetry of only the [O III]5007 emission line. They found very extended broad emission throughout their sample with the width containing the central 80 per cent of flux, $W_{80}$, ranging from 500 to 1800 km s$^{-1}$. This sample has a mean log($L_{[\mathrm{O\,III}]}$) luminosity of 43.2 erg s$^{-1}$. Similarly, Harrison et al. (2014) used the same technique on both the [O III]5007 and [O III]4959 emission lines to show that outflows were prevalent in their sample of 16 luminous type II AGN. Their AGN were required to be at $z < 0.2$ (with a mean $z = 0.1365$, and a mean log($L_{[\mathrm{O\,III}]}$) of 42.5 erg s$^{-1}$) and were selected to have broad (FWHM $> 700$ km s$^{-1}$), luminous emission components that must contribute $>30$ per cent of the flux. They too found extended broad emission with $W_{80}$ between 600 and 1500 km s$^{-1}$.

To further investigate the nature of outflows driven by AGN, we selected an unbiased sample of highly luminous local type II AGN to observe across a large spectral range at moderately high-spectral resolution. Observations were performed with the segmented pupil/image reformatting array lens (SPIRAL) IFU on the Anglo-Australian Telescope (AAT). A luminous sample was chosen to investigate winds at the extreme of the distribution. Additionally, no requirement for broad emission lines was applied to the sample, as was done in Harrison et al. (2014). Nearby galaxies were selected to allow for the best possible spatial resolution. In future work, this sample will be expanded and compared to galaxies observed by the SAMI Galaxy Survey (see Croom et al. 2012; Allen et al. 2014; Bryant et al. 2014) to better understand how feedback varies with AGN power and how these galaxies differ from their quiescent counterparts.

In this paper, we use a much larger spectral range than previous studies, allowing for fitting of the H$\beta$, [O III] $\lambda$5007, H$\alpha$, and [N II] $\lambda$6583 lines with a higher spectral resolution of $R_{\mathrm{blue}} = 2141$ and $R_{\mathrm{red}} = 5600$. This large spectral range also allows for multiple line ratios to be considered, meaning that ionization states of the winds can be derived using theoretical and observational cut-offs used in conjunction with diagnostic diagrams (Baldwin, Phillips & Terlevich 1981; Veilleux & Osterbrock 1987; Kewley et al. 2001; Kauffmann et al. 2003b). Our spectral range also captures many stellar absorption lines including the Calcium H and K lines at 3968.5 and 3933.7 Å, respectively. This enables measurements of the stellar populations and kinematics.

Primarily, the sample was selected and observed in order to learn more about AGN feedback. Using IFS data means that we are able to look for kinematic signatures of AGN feedback across the spatial extent of galaxies to see how these hosts are effected by the presence of the AGN. A key observation linked to AGN feedback is high-velocity gas, referred to as winds or outflows. To determine whether these are present, we must look for several signatures: broad emission lines, asymmetric line profiles, and high excitation. We expect winds to cause broad emission lines due to the large range in velocities of the swept-up gas, and the profile will likely be asymmetric as a result of the offset of the wind velocity. Additionally, we expect high ionization due to the winds being driven by the AGN or due to shocks caused as the outflow passes through the surrounding gas. In order to find these signatures, we fit multiple components to characterize the complex emission line profiles of our sample. We then use two approaches; the first is a non-parametric emission line analysis and the second considers the multiple components separately.

The outline of this paper is as follows: in Section 2, we describe the observations and data reduction process. Section 3 provides details of the kinematic analysis performed on the data, including the stellar and emission line kinematics, the statistics used to interpret our results, and the method used to obtain ionization diagnostics. In Section 4, we discuss the results of the analysis of our data. Section 5 considers the energetics of the outflows we observe, the implications of our results, and discusses a peculiar galaxy – J111100. In this paper, we adopt an $H_0 = 71$ km s$^{-1}$ Mpc$^{-1}$, $\Omega_{\mathrm{M}} = 0.27$, and $\Omega_{\Lambda} = 0.73$ cosmology.

## 2 OBSERVATIONS AND DATA REDUCTION

### 2.1 Target selection

The sample presented in this paper was selected to investigate the effects of feedback in luminous type II AGN by determining the fraction of these objects that show evidence of winds or outflows. We selected 17 highly luminous, local ($z < 0.11$) type II AGN from the SDSS DR7 (Abazajian et al. 2009) using spectral measurements from the MPA/JHU data base (Kauffmann et al. 2003a). According to the unified AGN model, the nuclei of type II AGN are obscured by a putative circumnuclear torus of dust, meaning that their spectra are dominated by narrow emission lines, typically with $\sigma < 1200$ km s$^{-1}$ (Antonucci 1993). Evidence now points to the dust obscuration being more clumpy (e.g. Nenkova et al. 2008; Hönig et al. 2013; Riffel, Storchi-Bergmann & Riffel 2014). However, this does not influence our selection which was chosen to get a clear view of the host galaxies of luminous AGN, relatively unhindered by the continuum emission from the nucleus. Using the luminosity of the [O III] $\lambda$5007 line within the 3 arcsec diameter SDSS fibre as a surrogate for the luminosity of the nucleus, targets were required to have log($L_{[\mathrm{O\,III}]}/\mathrm{L}_{\odot}$) $> 8.7$ to achieve a sample near the typical quasar–Seyfert luminosity boundary. To correct to a bolometric luminosity we use $L_{\mathrm{bol}}/L_{[\mathrm{O\,III}]} = 3500$ (Heckman et al. 2004), although we note that the scatter on this correction is large, ~0.38 dex. Using this correction, our [O III] luminosity limit corresponds to $L_{\mathrm{bol}} = 10^{12.2}\,\mathrm{L}_{\odot} = 10^{45.8}$ erg s$^{-1}$.

Baldwin-Phillips-Terlevich (henceforth BPT) diagrams (Baldwin et al. 1981) of log([O III]/H$\beta$) against log([N II]/H$\alpha$) were used to distinguish AGN, star-forming, and LINER-like (low ionization nuclear emission-line regions) systems (shown in Fig. 1). Targets were required to be above the theoretical star-forming limit described by Kewley et al. (2001; red dotted line in Fig. 1), in order

Downloaded from http://mnras.oxfordjournals.org/ at The Australian National University on July 12, 2016

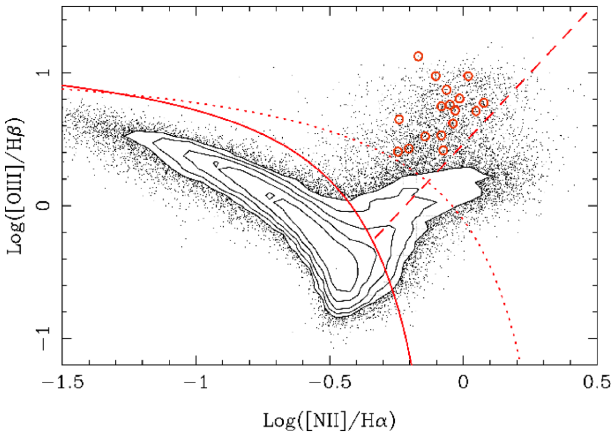


**Figure 1.** A BPT plot showing the selection criteria imposed on the sample. Red circles are the observed targets. The contours (logarithmically spaced) and black points show location of the full SDSS parent sample, and the red dotted line indicates the theoretical star-forming limit, from Kewley et al. (2001). The solid red line is the empirical AGN limit above which galaxies are considered to have an AGN contribution to their emission lines, and the dashed red line shows the division between true AGN and LINER-like emission, both from Kauffmann et al. (2003b).

that the [O III] luminosity did not have a significant contribution from star formation. Any objects with LINER-like line ratios were also rejected, meaning that they must lie above the diagonal dashed red line shown in fig. 1 taken from Kauffmann et al. (2003b).

The galaxies were required to have a redshift within the range $0.01 < z < 0.11$ (all fall within the range $0.05 < z < 0.11$). This was chosen to obtain the best possible spatial resolution, while still including sufficient high-luminosity AGN. A limit to declination $\delta < 10^{\circ}$ was also required to allow the objects to be observed from the AAT. The luminosity, BPT, redshift, and declination constraints resulted in sample of 149 AGN. We also prioritized objects with extinction corrections to the [O III] luminosity $A_{[\mathrm{O\,III}]} < 4$ (with the median of the sample being $A_{[\mathrm{O\,III}]} = 3.8$) to restrict the impact of uncertainty in the extinction correction on our [O III] luminosity (three objects are observed above this limit). From this final sample, we observed 17 AGN selected to have suitable right ascension at the time of observation and to be brighter than petrosian $r < 17.0$ in order to achieve a signal-to-noise ratio (S/N) of $\sim$10 Å$^{-1}$ pixel$^{-1}$ at $\lambda \approx$5500 Å at $R_{\mathrm{e}}$. The objects observed are shown in Fig. 1 as the red circles and details of each object are given in Table 1.

### 2.2 Observations

The targets were observed in 2011 March and April using the AAT's SPIRAL IFU. The SPIRAL IFU is a 512 element 16 × 32 rectangular array of fibres attached to the AAOmega spectrograph (Saunders et al. 2004; Sharp et al. 2006). Each fibre subtends 0.7 arcsec on the sky, approximately half the typical seeing.

As a result of the large field of view (FoV) of SPIRAL, a main difference between our data and the Harrison et al. (2014) data is the size of the IFU pointing. Our FoV covers an average of 915 kpc$^2$ compared to their 100 kpc$^2$. This means that while our spatial resolution is significantly poorer than theirs, we do capture the entire galaxy within the frame rather than just the central region. This difference will be important in later analysis as we consider different regions of the galaxies.

The AAOmega spectrograph splits the data into two arms (blue and red), resulting in two data cubes for each observed galaxy. The blue cubes encompass a wavelength range of 3700–5700 Å and the red from 6500 to 7600 Å. The red cubes have a higher resolution than the blue, with $R_{\mathrm{red}} = 5600$, while $R_{\mathrm{blue}} = 2141$, where $R = \lambda/\Delta\lambda$ and $\Delta\lambda$ is the full width at half-maximum (FWHM) of the spectroscopic point spread function (PSF). These resolutions

**Table 1.** A summary table of our observations. (1) IAU format name. (2)–(3) RA and DEC positions as taken from SDSS DR7. (4) SDSS redshift. (5) S/N of the H$\alpha$ line in the central spaxel as taken from our emission line fitting (described in Section 3.2.2); Galaxy J124859 has two values here as it was observed twice. (6) [O III] extinction derived from the Balmer decrement in the SDSS spectrum. (7) Extinction-corrected $\log(L_{[\mathrm{O\,III}]})$ in erg s$^{-1}$. (8) Galaxy stellar mass in units of log solar mass. (9) The extent of the observed two-component region, used to define the spatial extent of the outflow (see Section 5.1). (10) Average seeing during the observation measured in arcseconds. (11) Peak radio flux from FIRST measured in mJy. (12) Radio luminosity calculated from the FIRST flux, measured in W Hz$^{-1}$. (13) Mass of the central black hole in solar masses, as determined from the galaxy velocity dispersion. (14) Bolometric luminosity in erg s$^{-1}$, obtained from the [O III] luminosity.

| Object name (1) | RA (2) | DEC (3) | $z$ (4) | S/N (5) | $A_{[\mathrm{O\,III}]}$ (6) | $L_{[\mathrm{O\,III}]}$ (7) | $M_{\mathrm{star}}$ (8) | $D_{\mathrm{em}}$ (9) | Seeing (10) | FIRST (11) | $L_{\mathrm{FIRST}}$ (12) | $M_{\mathrm{BH}}$ (13) | $L_{\mathrm{bol}}$ (14) |
|---|---|---|---|---|---|---|---|---|---|---|---|---|---|
| J095155.34+032900.3 | 147.980 606 | 3.483 436 | 0.0601 | 30 | 5.63 | 42.3 | 11.0 | 3.3 | 3.0 | 1.78 | $1.55\times10^{22}$ | 7.70 | 45.85 |
| J101927.55+013422.4 | 154.864 822 | 1.572 914 | 0.0730 | 291 | 3.87 | 42.5 | 11.0 | 6.9 | 1.3 | 2.95 | $3.75\times10^{22}$ | 8.52 | 46.01 |
| J102143.30+011428.4 | 155.430 420 | 1.241 226 | 0.0787 | 269 | 3.21 | 42.5 | 10.8 | 6.3 | 2.7 | 1.97 | $2.93\times10^{22}$ | 8.62 | 46.06 |
| J103600.37+013653.5 | 159.001 556 | 1.614 885 | 0.1068 | 320 | 1.98 | 42.8 | 11.2 | 9.6 | 2.3 | – | – | 7.94 | 46.38 |
| J103915.69−003916.9 | 159.815 414 | −0.654 716 | 0.0770 | 208 | 2.98 | 42.4 | 10.5 | 7.2 | 2.1 | 30.34 | $4.31\times10^{23}$ | 7.40 | 45.98 |
| J111100.60−005334.8 | 167.752 533 | −0.893 009 | 0.0904 | 121 | 3.12 | 42.8 | 11.4 | 16.6 | 1.7 | 7.30 | $1.46\times10^{23}$ | 8.96 | 46.37 |
| J124321.32+005923.7 | 190.838 837 | 0.989 920 | 0.0834 | 114 | 3.15 | 42.3 | 10.8 | 8.8 | 2.0 | 1.01 | $1.70\times10^{22}$ | 7.53 | 45.87 |
| J124859.92−010935.4 | 192.249 680 | −1.159 850 | 0.0888 | 240,365 | 2.60 | 42.7 | 11.2 | 15.2 | 1.6,1.4 | 8.16 | $1.57\times10^{23}$ | 8.89 | 46.27 |
| J130116.09−032829.1 | 195.317 062 | −3.474 768 | 0.0864 | 396 | 2.89 | 42.4 | 10.8 | 11.4 | 1.4 | 1.96 | $3.55\times10^{22}$ | 7.67 | 45.94 |
| J133152.88+020059.2 | 202.970 367 | 2.016 448 | 0.0861 | 234 | 5.83 | 43.4 | 10.9 | 8.0 | 3.6 | 9.81 | $1.77\times10^{23}$ | 7.85 | 46.96 |
| J141926.33+013935.8 | 214.859 711 | 1.659 962 | 0.0764 | 190 | 3.34 | 42.8 | 10.9 | 7.1 | 1.5 | 4.69 | $6.56\times10^{22}$ | 7.59 | 46.35 |
| J142237.91+044848.5 | 215.657 990 | 4.813 485 | 0.0871 | 182 | 3.36 | 42.6 | 11.0 | 9.2 | 1.3 | 1.79 | $3.30\times10^{22}$ | 8.71 | 46.16 |
| J143046.02+001451.4 | 217.691 772 | 0.247 628 | 0.0546 | 270 | 3.81 | 42.5 | 11.2 | 6.7 | 2.5 | 9.47 | $6.55\times10^{22}$ | 8.38 | 46.05 |
| J150754.38+010816.7 | 226.976 593 | 1.137 990 | 0.0610 | 182 | 1.95 | 42.3 | 10.8 | 8.3 | 1.8 | 3.90 | $3.40\times10^{22}$ | 7.51 | 45.83 |
| J151147.47+033827.2 | 227.947 815 | 3.640 911 | 0.0780 | 187 | 3.76 | 43.1 | 10.9 | 8.3 | 1.6 | 6.94 | $1.01\times10^{23}$ | 7.65 | 46.61 |
| J152133.35−003628.5 | 230.388 977 | −0.607 926 | 0.0937 | 25 | 5.32 | 42.5 | 11.5 | 4.9 | 3.6 | 7.89 | $1.70\times10^{23}$ | 8.00 | 46.07 |
| J152637.67+003533.5 | 231.656 967 | 0.592 640 | 0.0507 | 187 | 3.09 | 42.5 | 10.9 | 6.3 | 2.3 | 3.80 | $2.25\times10^{22}$ | 7.49 | 46.03 |



Downloaded from http://mnras.oxfordjournals.org/ at The Australian National University on July 12, 2016

correspond to a velocity dispersion of $\sigma_{\rm red} = 23$ km s$^{-1}$ and $\sigma_{\rm blue} = 60$ km s$^{-1}$.

### 2.3 Data reduction

The raw data from SPIRAL were reduced using 2DFDR, an automatic data reduction program designed for use with the AAOmega multiobject spectrograph (Sharp & Birchall 2010). This package turns the raw CCD data received from the spectrograph into wavelength calibrated, sky-subtracted row-stacked spectra, with instrumental signatures removed.

The 2DFDR processing includes bias subtraction and dark subtraction, which removes a number of cosmetic features of the CCD in the blue arm of AAOmega. Flat-fielding is carried out at two levels, both using quartz lamp exposures. First, a set of flat-field exposures with a defocused spectrograph is used to provide relatively uniform illumination across the whole CCD. This is filtered to remove large-scale variations (e.g. colour response) but leave in pixel-to-pixel variations in CCD gain. The flat-field is then applied to the data prior to extraction of the spectra. Once the data are extracted to provide a spectrum per fibre (using a Gaussian fit to the spatial PSF of each fibre), a second stage of flat-fielding is applied, which uses an extracted fibre flat-field, which corrects each fibre to the mean wavelength response of the system. The relative calibration of the throughput of each fibre is done using twilight sky exposures. Wavelength calibration is carried out using fits to emission lines in arc lamp exposures (containing copper, argon, and iron) and results in residuals typically at the level of ∼0.1 pixels. Sky subtraction is carried out by constructing a mean sky spectrum from regions of the IFU around the edge of the array which do not contain flux from the target galaxy. Typically these were rows 1, 2, 31, and 32 in the 16 × 32 format of the SPIRAL IFU (although in some cases this was tuned to the geometry of the galaxy). The FoV of SPIRAL meant that we did not require extra offset sky exposures. After this processing, which results in row-stacked spectra, the data are aligned and combined into a data cube which places spectra at their observed $x$ and $y$ coordinates on the sky using a bespoke IDL routine. At all stages of the reduction, the variance information is propagated, resulting in a final variance cube to match the data cube.

Flux calibration and telluric correction were performed using standard stars which were observed together with the targets each night, allowing the shape of the spectra to be corrected for any instrumental or atmospheric effects. The range of airmasses for the observed targets was small, with a median of 1.25 and a maximum of 1.4. As a result, differential atmospheric refraction effects between the H$\alpha$ and H$\beta$ regions are significantly smaller (typically 0.25 arcsec, with a max of 0.44 arcsec) than both the IFU spaxel size and the atmospheric seeing (median 2.0 arcsec). Given this, and the extra spatial covariance in the noise properties of the data introduced by resampling (e.g. Sharp et al. 2014), we did not apply any correction for differential atmospheric correction. To account for transmission variations through the night, we then compare our data cubes to the SDSS spectra for each object. We create a summed spectrum from an aperture of diameter 3 arcsec to match the SDSS fibre aperture and then apply a simple scaling of our cubes to match the normalization of the SDSS spectra.

## 3 SPECTRAL ANALYSIS

In this section, we will discuss the analysis of the kinematic properties of the galaxies within our sample. As previously discussed, we expect the kinematics to contain information about the environment within these galaxies and how the AGN is affecting it. In particular, we want to find evidence for disturbances within the galaxies to show that outflows may be present. To do this, we examine the stellar and gas kinematics first to observe how the galaxies are rotating, and further to see if the gas kinematics show signs of disruption by the AGN (as the stars will not be effected by winds). In Section 3.1, we discuss the fitting of the stellar populations of the galaxies which were used to constrain the stellar motion allowing for the continuum of the galaxies to be subtracted. In Section 3.2.1, we discuss the first method used to look for signatures of winds, focusing on line broadness and asymmetry. Finally in Section 3.2.2, we will explain the method used by our fitting routine LZIFU (Ho et al., in preparation) and how we use it to separate out broad components in the spectra that are likely to represent winds.

### 3.1 Stellar kinematics

We fit the stellar kinematics of the sample using the penalised pixel fitting (PPXF) algorithm developed by Cappellari & Emsellem (2004). This routine uses simple stellar population (SSP) synthesis to fit both the velocity and velocity dispersion of the stars within the galaxy.

In this paper, we made use of the high-resolution Gonzalez Delgado SSP template library from Martins et al. (2005) and González Delgado et al. (2005).[1] We selected nine solar metallicity templates aged between 0 and 17 Gyr to fit to our spectra. We run PPXF on a spatially smoothed (3 pixel boxcar kernel) version of our data as the low S/N in the outskirts of the galaxies means that the velocities are poorly constrained. To retrieve the best possible fit to the velocities (disregarding all other information), we use a multiplicative polynomial of order eight and an additive polynomial of order 3 in addition to the templates which results in the most spatially continuous velocity maps possible. From this fit, only stellar velocities are extracted, we do not consider the stellar dispersions. PPXF is then run in conjunction with our emission line fitting (within the LZIFU software) on the unsmoothed data to produce a best-fitting stellar template made up of a linear combination of the input templates with an appropriate velocity and velocity dispersion. During this run only the reddening keyword is used to account for dust, as in this case we are concerned with the exact continuum absorption. This information was then used to subtract the stellar component of the spectra, a necessary step to correct emission line fluxes for stellar absorption (particularly the Balmer lines). We note that because our emission lines are typically very strong, our results are not sensitive to the details of the continuum correction.

Derivation of the stellar kinematics also allowed us to observe the differences between the stellar and gaseous kinematics. This is useful as gas and stars react differently to disturbances within the host galaxy, such as feedback from the AGN or interactions with nearby galaxies. Due to their non-collisional nature, the stars are more immune to these effects and tend to reflect the overall gravitational potential of the galaxy, while gas is easily disrupted from ordered rotation. Since a wind will have no impact on the kinematics of the stars, these differences may be used to determine whether the wind is significantly disturbing the gas rotation.

[1] The library was based on atmosphere models from PHOENIX (Hauschildt & Baron 1999; Allard et al. 2001) and ATLAS9 computed with SPECTRUM (Gray & Corbally 1994). The ATLAS9 library is computed with SYNSPEC and TLUSTY (Lanz & Hubeny 2003).

Downloaded from http://mnras.oxfordjournals.org/ at The Australian National University on July 12, 2016

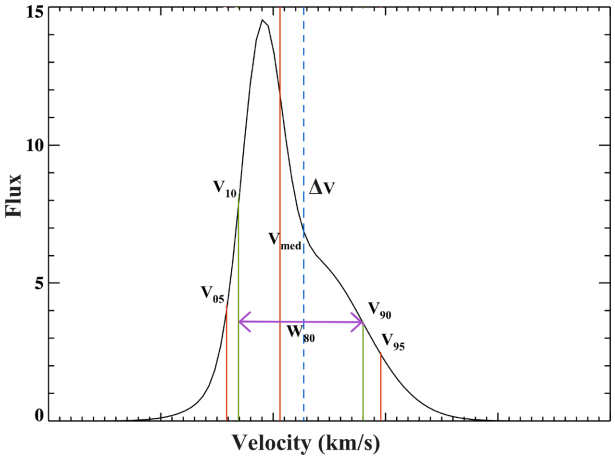


**Figure 2.** A visualization of the non-parametric measurements used in this paper. Plotted in black is an example fit to an emission line. The overplotted lines represent the calculated velocities for the fit. The first is $v_{05}$ (red) – the velocity at 5 per cent flux, $v_{10}$ (green) – the velocity at 10 per cent flux, $v_{\rm med}$ (red) – the median velocity, $\Delta v$ (dashed blue line) – as defined in equation (2) is a measure of the asymmetry of the line profile, $v_{90}$ (green) – the velocity at 90 per cent flux, and $v_{95}$ (red) – the velocity at 95 per cent flux. $W_{80}$ is defined as $v_{90} - v_{10}$ which is the width that contains 80 per cent of the flux, shown by the purple arrow.

### 3.2 Emission line analysis

It is well established that the structure of emission lines in the central regions of AGN is very complex, often possessing apparent multiple velocity components along the line of sight (e.g. Villar-Martín et al. 2011; Veilleux et al. 2013). Examples of these complex structures may be seen in the bottom panels of Figs 3 and 4, where distinct kinematic components are evident either in the form of offset narrow and broad components (Fig. 3) or two narrow components making up a horned profile with underlying broad wings (Fig. 4). While it has been suggested that emission lines with this double-peaked signature were due to the presence of two distinct AGN (Comerford et al. 2013), it has been demonstrated that an outflow with an uneven velocity distribution can lead to this profile (e.g. Fischer et al. 2011). In order to gain better understanding of outflows, we must disentangle these distinct components.

Two commonly used methods will be used to analyse fits to the AGN emission lines, the first is a non-parametric approach (see Fig. 2; Liu et al. 2013; Harrison et al. 2014) and the second considers these multiple components as signatures of the physical gas dynamics (e.g. Ho et al. 2014). To model the emission profiles present in the data, we used up to three Gaussian components for each emission line, requiring statistical significance above a chosen threshold to justify the higher order model (see Section 3.2.3).

#### 3.2.1 *Non-parametric emission line measures*

Emission line properties may be derived using non-parametric line measures derived from the summed model fit produced by our multiple component fitting routine. We use the model spectra to counter low S/N in the outer parts of the galaxies and to separate out the H$\alpha$ and [N II] emission which is often blended. When using non-parametric measures, we do not separate out components within the spectra (i.e. we do not separate the multiple Gaussian components), but instead use them to characterize the profile by making the measurements based on the summed model spectra. To do this, several definitions from the literature are used, allowing us to compare our results to those found previously. A visualization of these measures is shown in Fig. 2. The definitions are as follows.

(i) The median velocity of the primary emission line (H$\alpha$) is defined as the velocity that bisects the area under the fit, and is denoted $v_{\rm med}$. Asymmetry of the line profile is measured from this value.

(ii) $v_{05}$, $v_{10}$, $v_{90}$, and $v_{95}$ are defined as the velocities at 5, 10, 90, and 95 per cent of the line flux, respectively.

(iii) The non-parametric line width, $W_{80}$, is defined as the width that contains the central 80 per cent of the flux:

$$W_{80} = v_{90} - v_{10}. \quad (1)$$

For a Gaussian, it is approximately the FWHM ($W_{80} = 1.09$ FWHM for a Gaussian), and is used as a more sensitive measure of the broadness of the emission lines.

(iv) Finally, an asymmetry parameter (modified from Harrison et al. 2014) is used to aid in comparison to their results. We define $\Delta v$ as

$$\Delta v = \frac{v_{05} + v_{95}}{2} - v_{\rm med}. \quad (2)$$

This asymmetry parameter allows for the velocity of the underlying broad component to be traced across the galaxy to examine the direction of the outflow.[2]

The Harrison et al. (2014) definition of $\Delta v$ uses the peak velocity of their primary emission line, [O III]. In place of this, we use the median velocity as the zero velocity point, as done in Liu et al. (2013). We chose to do this as the peak velocity is not smoothly varying with spatial location in the majority of our sample due to the prominent double-peaked emission lines in the centre of the galaxies (e.g. the spectra shown in Fig. 4). As a result of this, the peak velocity shows non-physical gradients as the double-peaked profiles vary rapidly in flux. We do not, however, claim that the median velocity of the line traces the velocity of the outflow as stated in Liu et al. (2013). Comparison with the stellar kinematics (see Appendix A) demonstrates that this value is in fact qualitatively closer to the overall rotation of the galaxies in most of our sample. In 9/17 galaxies, we see evidence for large-scale consistent rotation in both the gas and stars (e.g. J101927 and J124321, shown in Fig. A2 and Fig. A7 in Appendix A). 8/17 galaxies show different gas and stellar rotation, of these 6 were found to be in identifiable mergers (e.g. J143046, Fig. A13, or J111100, Fig. A6), while 1 is a barred spiral (J142237, Fig. A12), and 1 is a regular-looking spheroidal.

#### 3.2.2 *Emission line fitting procedure*

When dealing with complex emission or absorption-line spectra, the standard approach is to use a function made up of multiple Gaussians. However, it is still an open question as to what should be done with these multiple component fits and how they should be interpreted. One approach states that nothing physically meaningful should be extracted from these fits, and that they are only needed to account for our inability to model non-Gaussian emission lines. If this is the stance taken, the appropriate solution is to use non-parametric emission line measures as done in much of the literature (e.g. Liu et al. 2013; Veilleux et al. 2013; Harrison et al.

[2] A similar asymmetry parameter is used by Liu et al. (2013), originally defined by Whittle (1985). It produces qualitatively the same results, but is a ratio of velocities rather than a velocity. We chose to use $\Delta v$ as it is conceptually easier to understand as a velocity.



Downloaded from http://mnras.oxfordjournals.org/ at The Australian National University on July 12, 2016

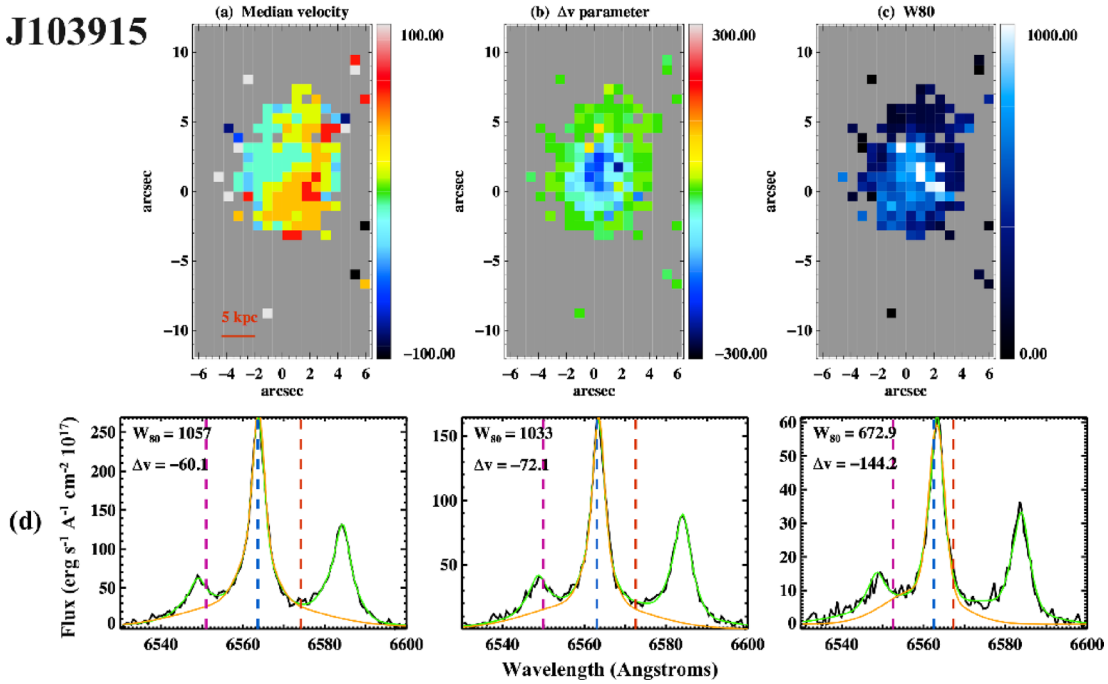


**Figure 3.** An example of non-parametric emission line measures for J103915. (a) $v_{\rm med}$ is the median velocity (km s$^{-1}$) of the emission line, which is shown graphically on the spectra below as the blue dotted line. It is evident here that this galaxy shows only slight rotation (with velocity varying to approximately ±45 km s$^{-1}$ on either side of the galaxy), meaning that it may be relatively face-on. (b) $\Delta v$ parameter, blue represents a blueshifted asymmetry in the line profile, while green indicates no asymmetry. (c) $W_{80}$ is mapped in blue with increasing line width as the colour lightens. It is clear that this object is broader in the centre, with $W_{80}$ exceeding 1000 km s$^{-1}$. (d) The data and the H$\alpha$ fit for three adjacent central spaxels are plotted. The data are in black, the total fit is overplotted in green, the H$\alpha$ component of the fit only is plotted in orange. Several velocity measures are also plotted, purple is $v_{10}$ (velocity that bounds 10 per cent of the flux), blue is the median velocity (velocity at 50 per cent flux), and in red is $v_{90}$. Values for $W_{80}$ and $\Delta v$ are printed in the top-left corner of the plots.

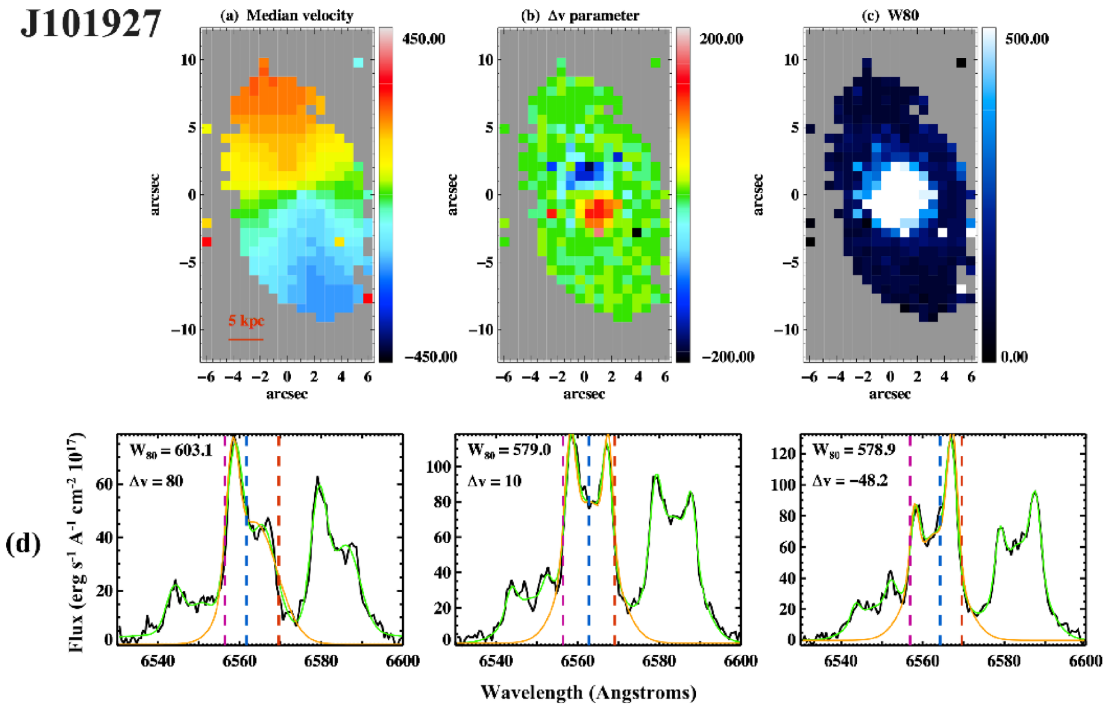


**Figure 4.** All figure placements are the same as the above. This example serves to highlight how non-parametric measures do not fully capture the double-peaked features of the spectra. In panel (d), the double-peaked emission lines can clearly be seen; here, by only using the summed fit, we are discarding extra information contained in the three-component fit to the horned profile.

Downloaded from http://mnras.oxfordjournals.org/ at The Australian National University on July 12, 2016

2014). However, examination of our sample shows that distinct spatially varying velocity components are present in the majority (e.g. double-peaked lines). As a result, we decided to model these components separately and to investigate whether they possessed any meaningful physical information (centroids, ionization, velocity, dispersion) as was done in Ho et al. (2014).

We used LZIFU, an emission and absorption-line fitting program developed by Ho et al. (in preparation) to model the emission line kinematics using single and multiple Gaussian profiles. LZIFU first subtracts the stellar continuum of the galaxies using PPXF (in this case, using only the reddening keyword to correct for the presence of dust), and then fits the emission lines using MPFIT. This software has the capability to simultaneously fit the red and blue spectra taking into account the differences in resolution. Additionally, this feature allows for the typical BPT line diagnostics to be performed on the multiple component fits.

Each set of emission lines was modelled with a set of Gaussian functions constructed using the known wavelength values of each line. The central wavelength of the most prominent line ([O III]5007 in the blue or H$\alpha$ in the red) was allowed to vary up to a velocity of 600 km s$^{-1}$ and the velocity dispersion up to 2000 km s$^{-1}$. We then add up to two more sets of Gaussians to the fit, meaning that each emission line is modelled by up to three Gaussian components. To constrain the fit, each set of Gaussians was required to have the same velocity and velocity dispersion (meaning that their relative wavelengths were fixed), while their fluxes were allowed to vary. The reasoning for this is that each component represents a kinematically distinct part of the gas, meaning that they may have different ionization states determined by their relative fluxes. This meant that, for example, the single-component set of Gaussians fit to the red data (encompassing the [N II], H$\alpha$, and [S II] lines) instead of having fifteen free parameters, only had six (a single velocity and velocity dispersion, flux of the H$\alpha$ line, one flux defining the stronger [N II] line, with the weaker line being locked to 1/3 of the stronger line's flux, and two fluxes for the [S II] doublet).

It should be noted that LZIFU sorts components by dispersion. So for every spaxel, component 1 is always the narrowest, component 2 is always the medium dispersion component, and component 3 is the broadest. Because of this, whenever we are discussing a wind or outflowing component, we are primarily referring to component 3 (or component 2 if only two components are required as in J095155 and J124321) as this will have the greatest wind contribution.

#### 3.2.3 Model selection

To determine if the multiple components detected are statistically significant, and not a better fit purely by virtue of the extra model parameters, we performed a series of *f*-tests. The *f*-test is a standard statistical test to gauge whether a higher order model is preferable to a simpler model when fitting a particular data set. We set the false rejection probability for the lower order model to $10^{-5}$ (corresponding to an $\sim 3.9\sigma$ requirement that the more complex model is preferred). This choice of probability results in spatially contiguous regions of preferred number of components. Adjusting it higher results in nosier component maps, while adjusting it lower only slowly reduces the regions where the more complex models are preferred. This means that the higher this threshold is set, the harder it is to justify the more complex model.

Once the preferred number of components for each spaxel of the galaxy has been determined, maps of this preference in each spaxel can be made as shown in the top left of Fig. 5. By producing this, we are able to see where spatially these multiple components lie, and to only examine the appropriate multiple component fits in these regions.

#### 3.2.4 Ionization diagnostics

The ratios of the intensity of prominent emission lines may be used to determine the dominant ionizing source, whether it be ionization from young stars, from a power-law accretion disc or from shock heating (Baldwin et al. 1981). Due to their differing ionizing spectra, softer ionizing sources such as star formation tend to excite permitted emission such as the hydrogen Balmer lines, and harder ionizing sources excite greater emission in forbidden lines such as [N II] and [O III] leading to greater flux in these lines.

From the single-component emission line fits discussed in the previous section, we can construct BPT diagrams for each of the galaxies, as shown in Fig. 6. In addition to this, BPT maps of the ionization states across the spatial projection of the galaxies can be made, as seen in the top right of Fig. 5.

We are also able to determine the ionization states of the multiple components present in the central regions of the galaxies. We produce BPT diagrams and maps for each of the three components. We also plot the velocity dispersion of the three components versus their log([N II]/H$\alpha$) line ratio following Rich, Kewley & Dopita (2011) and Ho et al. (2014) to see how the components separate out in this parameter space, as shown on the right of Fig. 6. By comparing dispersion to ionization state, we are testing for evidence of shocks as they are known to cause a strong correlation between the two (Dopita & Sutherland 1995).

## 4 RESULTS

### 4.1 Non-parametric emission line measures

We measured the value of $W_{80}$ for the emission lines in the central regions of our galaxies (defined as either the two- or three-component region dependent on the maximum number of components required for each galaxy, as listed in Table 2). The results of this are shown in columns (6) and (7) of Table 1. Column (6) contains the mean $W_{80}$ in the central region of the galaxy and column (7) shows the maximum width within the spatially contiguous maximum component region. From this, we find that our sample shows $W_{80,\,\mathrm{max}} \approx 400$–1600 km s$^{-1}$, with an average of $794 \pm 90$ km s$^{-1}$. This is significantly higher than is expected for quiescent galaxies whose central regions would generally have $W_{80} < 400$ km s$^{-1}$ (e.g. Vega Beltrán et al. 2001). Since this broadness may not be attributed to normal rotation, we must conclude that it is plausibly due to either outflowing gas driven by the AGN or dynamical disturbances caused in merging systems (though we do not expect this to be so centrally peaked if it is due to merging, as we observe in our sample).

We may directly compare these results to previous studies performed by Harrison et al. (2014) and Liu et al. (2013) who measure $W_{80}$ of the [O III] emission lines. Harrison et al. (2014) find very similar results, with $W_{80,\,\mathrm{max}}$ ranging from 720 to 1600 km s$^{-1}$. Since our galaxies have similar luminosities, we expect our results to be in agreement, and this is mostly true though Harrison's results are slightly higher. This may be attributed to their selection methods, which required a significant broad component with FWHM $> 700$ km s$^{-1}$ to be present leading to their lowest $W_{80,\,\mathrm{max}}$ being around that value (as $W_{80} = 1.09$ FWHM). Since we did not make such a selection, our sample also contains some galaxies with narrower emission lines.



Downloaded from http://mnras.oxfordjournals.org/ at The Australian National University on July 12, 2016

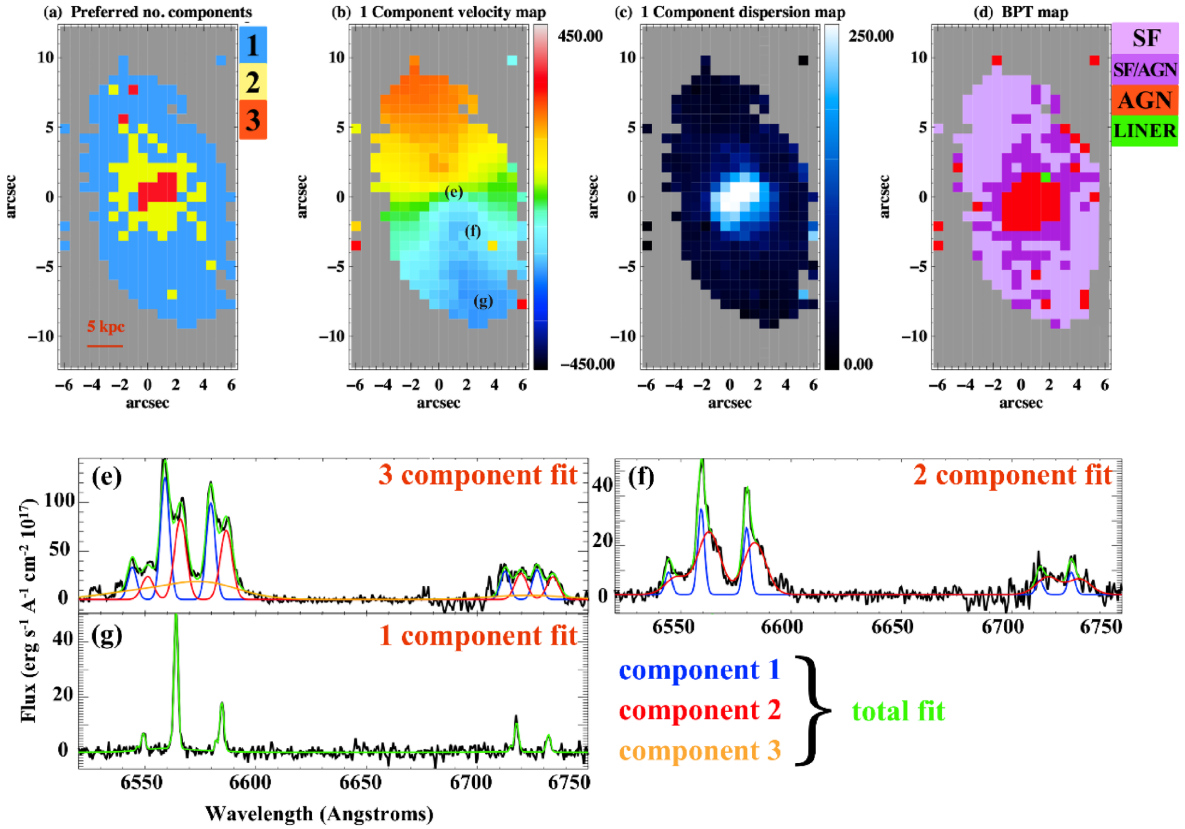


**Figure 5.** An example of the results of a multiple-component fit for galaxy J101927. (a) A component map showing the number of components required. Grey represents data that does not meet the S/N cut (S/N > 3 in [N II] and H$\alpha$), blue is regions that require only one component, yellow is regions that require two components, and red is regions that require three components. (b) and (c) One-component velocity and velocity dispersion maps for the whole galaxy. These are derived from the single Gaussian fit that is performed on all the data. While this is qualitatively similar to $v_{\rm med}$, it is not the same and is derived in a different way. (d) A BPT map, made using a BPT diagnostic plot from the line ratios log([N II]/H$\alpha$) and log([O III]/H$\beta$), by classifying each spectrum then projecting the classification back on to the spatial dimensions of the galaxy. Here, light purple represents star formation-dominated ionization, purple is the composite region of the BPT diagram, and red is AGN. Shown are three example spectra for each component region of the galaxy. Approximate locations of the spaxel containing each spaxel are marked on the velocity map. (e) Three-component fit where components 1, 2, and 3 are shown in blue, red, and orange, respectively, with the total fit overplotted in green. (f) Two-component fit with components one and two plotted in blue and red, with the total fit in green. (g) One-component fit with only the green line representing the total fit. Distinct differences in the spectra are seen as the complexity of the emission lines increases greatly in the three-component region.

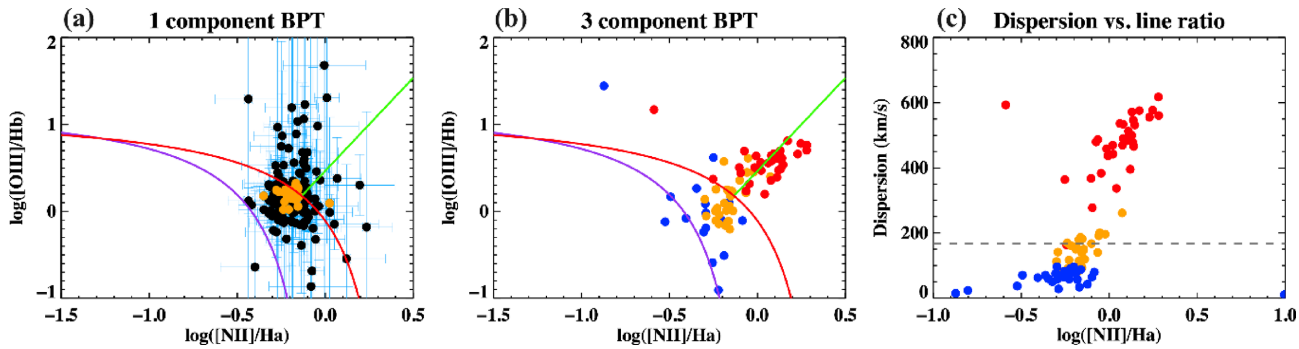


**Figure 6.** (a) A standard one-component BPT diagram for J133152 with diagnostic lines overplotted. Points from the three-component region are colour-coded orange. The observed star formation cut-off from Kauffmann et al. (2003b) is plotted in purple, while their LINER classification line is in green. The red line shows the maximum theoretical starburst ionization calculated by Kewley et al. (2001). The orange points are the spaxels from the three-component region, but fitted with a single Gaussian, whose three-component fits are then used in the following plots. We see that their one-component fits place them clustered on the border of the AGN, LINER, and composite regions, but when the three-component fits are examined we see clear trends between dispersion and ionization. (b) A BPT diagram showing the location of each of the three components fitted in the centre of J133152. The blue points are component 1, orange are component 2, and red are component 3. (c) Velocity dispersion plotted against log([N II]/H$\alpha$) line ratio, demonstrating the trend of increasing line ratio with dispersion indicative of a contribution from shocks. The colour coding of the points is the same as in (b). The dashed grey line shows the median stellar dispersion within the three-component region to demonstrate where gas dispersions are significantly higher than this value.

Downloaded from http://mnras.oxfordjournals.org/ at The Australian National University on July 12, 2016

**Table 2.** A summary table of the results obtained from the sample. (1) Shortened galaxy name. (2) Class, a galaxy classification, I – isolated, the galaxy has no near neighbours. P – an interacting pair, a galaxy undergoing a merger with a companion. T – tidal tails, a galaxy with prominent tidal features. (3) Optimal number of components required in the central region of the galaxy (which is henceforth defined as the three- or two-component region of the galaxy depending on the value listed in column. (4) log(H$\alpha$) luminosity in erg s$^{-1}$ derived from our multiple component fits to emission lines within $D_{\rm em}$ as listed in Table 1. (5) $W_{80}$ is the line width containing 80 per cent of the flux derived from fits to the H$\alpha$ line. The value listed is the median within the central region of the galaxy. (6) The maximum value of $W_{80}$ within the spatially coherent maximal-component region. (7) $|\Delta v|$ is absolute value of the asymmetry parameter defined in equation (2), the value listed is the median within the central region of the galaxy. (8) The maximum of the absolute value of $\Delta v$ within the central region of the galaxy. (9), (10), (11) Median velocity of component 1, 2, and 3 from the emission line fitting. If only two components are required, then only components 1 and 2 are listed. Errors on these values are typically 2 per cent for component 1, 6 per cent for component 2, and 30 per cent for component 3. (12), (13), (14) Median dispersion for each component. Errors on these values are typically 4 per cent for component 1, 4 per cent for component 2, and 6 per cent for component 3. (15) The Spearman's rank coefficient for the correlation between velocity dispersion and [N II]/H$\alpha$ line ratio. (16) The probability of the observed correlation given the number of data points.

| Galaxy (1) | Class (2) | Comp (3) | $L_{\rm H\alpha}$ (4) | $W_{80}$ (5) | $W_{80,\,\rm max}$ (6) | $\lvert\Delta v\rvert$ (7) | $\lvert\Delta v\rvert_{\rm max}$ (8) | $v_1$ (9) | $v_2$ (10) | $v_3$ (11) | $\sigma_1$ (12) | $\sigma_2$ (13) | $\sigma_3$ (14) | SRC (15) | Prob. (16) |
|---|---|---|---|---|---|---|---|---|---|---|---|---|---|---|---|
| J095155 | P | 2 | 43.18 | 317 | 415 | 37 | 195 | 133 | 68 | – | 37 | 114 | – | 0.43 | 0.24 |
| J101927 | I | 3 | 43.13 | 555 | 579 | 48 | 229 | −176 | 184 | 11 | 48 | 71 | 238 | 0.43 | 0.01 |
| J102143 | I | 3 | 42.72 | 576 | 1152 | 60 | 228 | −152 | 41 | 19 | 68 | 159 | 1072 | 0.61 | $3.18\times10^{-5}$ |
| J103600 | P | 3 | 43.21 | 491 | 585 | 47 | 281 | 189 | −9 | −27 | 72 | 110 | 330 | 0.44 | $2.05\times10^{-4}$ |
| J103915 | I | 3 | 43.21 | 673 | 1057 | 96 | 240 | 34 | 35 | −81 | 42 | 126 | 419 | 0.63 | $1.29\times10^{-6}$ |
| J111100 | T | 3 | 43.46 | 736 | 1116 | 36 | 202 | −185 | 61 | −93 | 70 | 148 | 363 | 0.05 | 0.55 |
| J124321 | I | 2 | 43.33 | 406 | 645 | 72 | 299 | −6 | 8 | – | 81 | 269 | – | 0.52 | $1.76\times10^{-5}$ |
| J124859 | T | 3 | 43.25 | 927 | 1569 | 48 | 178 | 22 | 33 | −67 | 68 | 202 | 515 | 0.23 | 0.01 |
| J124859_a | T | 3 | 43.39 | 903 | 1617 | 48 | 250 | 34 | 45 | −44 | 60 | 198 | 539 | 0.32 | $9.08\times10^{-5}$ |
| J130116 | P | 3 | 43.84 | 334 | 405 | 60 | 167 | 123 | −5 | −48 | 49 | 88 | 361 | 0.71 | $3.76\times10^{-27}$ |
| J133152 | T | 3 | 43.50 | 834 | 1001 | 250 | 334 | −27 | 21 | −336 | 64 | 140 | 487 | 0.70 | $3.82\times10^{-16}$ |
| J141926 | T | 3 | 43.40 | 385 | 529 | 60 | 204 | 79 | −11 | −151 | 55 | 99 | 342 | 0.64 | $3.63\times10^{-16}$ |
| J142237 | I | 3 | 43.56 | 476 | 714 | 71 | 214 | −14 | −57 | −28 | 42 | 74 | 253 | 0.52 | $7.99\times10^{-10}$ |
| J143046 | P, T | 3 | 43.39 | 565 | 687 | 25 | 245 | −247 | 53 | −48 | 71 | 142 | 415 | 0.24 | 0.04 |
| J150754 | I | 3 | 42.67 | 488 | 659 | 37 | 220 | 50 | −11 | 19 | 55 | 102 | 307 | 0.36 | $8.75\times10^{-4}$ |
| J151147 | I | 3 | 43.43 | 408 | 528 | 36 | 240 | 102 | −2 | −18 | 65 | 94 | 283 | 0.61 | $5.48\times10^{-12}$ |
| J152133 | T | 1 | 42.87 | 331 | 520 | 59 | 154 | −110 | – | – | 115 | – | – | 0.20 | 0.25 |
| J152637 | I | 3 | 42.88 | 468 | 517 | 37 | 148 | 106 | −107 | −36 | 44 | 98 | 226 | 0.08 | 0.34 |

Liu et al. (2013) also find similar, but slightly larger, values; $W_{80,\,\rm max} \approx 525$–2142 km s$^{-1}$. Here, it should be noted that this sample is at a considerably higher redshift than ours, $z \approx 0.55$, and that they were therefore able to select more luminous targets. Our widths were measured using the H$\alpha$ rather than the [O III] emission line, which may introduce a slight difference as we are comparing a permitted emission line width to a forbidden width. However, since in the fitting code the velocity dispersion of the Balmer and forbidden lines are tied, we do not expect this to introduce a large difference except in objects with significant contributions from the broad-line region (BLR; e.g. J102142).

In Fig. 7, we plot the results from our sample (blue), Harrison et al. (2014, red), and Liu et al. (2013, green). The three values we consider are $W_{80,\,\rm max}$ (the maximum value of $W_{80}$ within the spatially contiguous three-component region), $|\Delta v|_{\rm max}$ (the maximum value of $\Delta v$ within the spatially contiguous three-component region), and the [O III] luminosity from SDSS. It is apparent from these plots that there is no correlation between the parameters in the available data, despite the large range of luminosities across the three samples. This is not wholly unexpected as Mullaney et al. (2013) show that while there is a strong trend between line width (FWHM) and [O III] luminosity across a large range of luminosities, at the highest luminosities ($L_{\rm [O\,III]} > 10^{42}$) objects show a large variety of line widths. Since we made no selection to preferentially observe objects known to have moderately broad lines, we likely selected a larger number of these high-luminosity, low-line-width objects than Harrison et al. (2014).

Three galaxies show strong blueshifted wings in their centre indicative of an outflow directed towards the observer. An example of this is shown in the centre of the top row of Fig. 3 ($\Delta v$ map) where velocities close to zero are represented by green, negative offset in velocity is bluer, and positive offset in velocity would be redder. It is clear in this example that there is a central blue asymmetry in the emission lines, which is coincident with very broad emission lines (evident from the centrally high $W_{80}$ shown to the right of the top row of Fig. 3), which indicates an outflow. This observation is supported by these galaxies showing low-amplitude ($<100$ km s$^{-1}$) rotation potentially due to a close to face-on inclination, meaning that an outflow perpendicular to the disc would be directed along the line of sight to the observer.

Both Harrison et al. (2014) and Liu et al. (2013) find a larger fraction of galaxies with blueshifted asymmetries (around 30 per cent of their samples) and a slightly lower fraction showing rotation-like gradients (between 31 and 43 per cent). Due to the very similar selection methods, we expect to see the same trends; however, asymmetry is more closely tied to the geometry and orientation of the target galaxies on the sky. In the case of the Harrison et al. (2014) sample, this may be the result of their selection criteria, which required a broad (FWHM $> 700$ km s$^{-1}$) component. Since the greatest apparent dispersion will be seen when an outflow is viewed face-on (if it is not spherically symmetric), selecting for broadness may bias a sample towards face-on outflows. When the errors on the percentages shown in Table 3 are considered, the difference between our conclusions becomes less stark, as the errors are large due to the small sample sizes. Our values then mostly agree, but we do still see a greater fraction of $\Delta v$ gradients. It is noted that the lower number of galaxies showing large-scale rotation in the Harrison et al. (2014) sample is potentially a result of their much smaller FoV.



Downloaded from http://mnras.oxfordjournals.org/ at The Australian National University on July 12, 2016

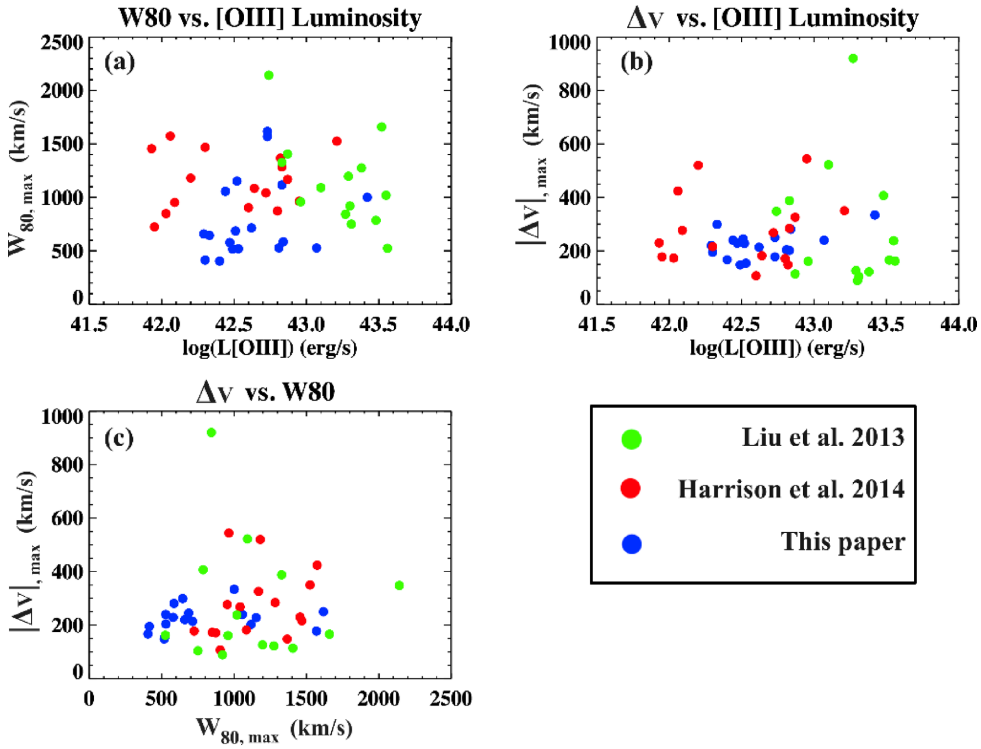


**Figure 7.** Plots comparing emission line measures from this sample, Harrison et al. (2014), and Liu et al. (2013). Panel (a) plots $\log(L_{[\mathrm{O\,III}]})$ luminosity against $W_{80,\,\mathrm{max}}$; it is apparent that there is no correlation between the two. (b) $|\Delta v|_{\mathrm{max}}$ is plotted against $\log(L_{[\mathrm{O\,III}]})$; again no correlation is seen. Panel (c) shows $|\Delta v|_{\mathrm{max}}$ versus $W_{80,\,\mathrm{max}}$; there is still no clear correlation.

**Table 3.** A table showing the occurrence of rotation, gradients in $\Delta v$, blueshifted $\Delta v$, and double-peaked emission lines within the three samples. The sample discussed in this paper has the highest occurrence of large-scale rotation, $\Delta v$ gradients, and double-peaked emission lines. It also shows the lowest occurrence of blueshifted $\Delta v$. Binomial errors are shown in each case. It should be noted that the much smaller IFU pointing that only captures the central region of many targets in Harrison et al. (2014) may be the reason for the lower number of galaxies that show evidence for rotation. This is because without seeing the extended disc or outskirts of the galaxies it can be difficult to tell if there is large-scale rotation.

| Sample | Large-scale rotation | $\Delta v$ gradient | Blue $\Delta v$ | Double peaked |
|---|---|---|---|---|
| Harrison et al. (2014) | 50 ± 13 per cent | 31 ± 12 per cent | 31 ± 12 per cent | 19 ± 10 per cent |
| Liu et al. (2013) | 71 ± 14 per cent | 43 ± 15 per cent | 28 ± 14 per cent | 0 per cent |
| This paper | 76 ± 10 per cent | 65 ± 12 per cent | 17 ± 9 per cent | 41 ± 12 per cent |

In Table 3, we list the percentages of galaxies from this sample, Harrison et al. (2014), and Liu et al. (2013) that have apparent large-scale rotation, $\Delta v$ gradients in the opposite direction to the galactic rotation, and double-peaked emission lines. We see $\Delta v$ gradients opposite to the rotation across the major axis of a large fraction of our sample (65 ± 12 per cent). This is not what we expect from an outflow perpendicular to the disc due to the varied inclinations of the sample all showing the same signature. The gradients in $\Delta v$ are only seen in galaxies that have what appears to be large-scale rotation [the same is true of the Harrison et al. (2014) and Liu et al. (2013) samples]. This signature would be a natural consequence of beam smearing, due to atmospheric seeing combined with a velocity gradient across the field and a strong centrally peaked flux distribution. However, beam smearing cannot be used to explain the complex multicomponent structure in the central, most luminous spaxels, as these would naturally be less impacted by beam smearing. The galaxies that show $\Delta v$ gradients also tend to have resolved multiple components in their central (and surrounding) spaxels. It is the changing contributions of these different components that appears to drive the $\Delta v$ gradients.

Due to the uncertainty in the meaning of $\Delta v$, we do not use it in any calculations or reasoning. Since $W_{80}$ is centrally peaking, it is much less affected by this issue, and the observed broadness is much greater than could be achieved by beam smearing of a regularly rotating disc. So when discussing outflow velocities, we rely on our $W_{80}$ measurements. Full kinematic modelling of these galaxies including the effects of disc rotation, winds, seeing, and beam smearing will be undertaken in a later paper. The typical seeing is ≈2 arcsec and exact values for each object are tabulated in Table 1.

We find that all of the galaxies show abnormalities in their emission in the form of extremely broad and asymmetric lines. These properties are not expected of normal rotating discs, or even of luminous high-redshift mergers whose line widths are generally

Downloaded from http://mnras.oxfordjournals.org/ at The Australian National University on July 12, 2016

$<600\,\mathrm{km\,s^{-1}}$ (e.g. Harrison et al. 2012). These properties are generally taken to be signatures of high-velocity outflows in the gas (see Heckman et al. 1981; Liu et al. 2013; Harrison et al. 2014).

### 4.2 Multiple components

Pieces of evidence for multiple components that meet both the requirements for statistical significance (outlined in Section 3.2.3) and are extended on scales greater than the spatial resolution (almost 3 spaxels, or ≈2 arcsec) were found to be present in all but one of the sample, with the majority preferring a three-component fit in their central region. A visualization of this can be seen in Fig. 8 where the spatial maps of where each number of components are required for the whole sample are shown. It should be noted that the one galaxy that does not show evidence for multiple components has the poorest data of the entire sample, with a central S/N 10 times lower than the average (J152133 in Fig. 8). Additionally, the galaxies that show mainly two components, seen in Fig. 8 (J095155 and J124321), also have low S/N (tabulated central S/N values may be found in Table 1). The poor S/N of the data for these galaxies is likely partially due to the observing conditions, with seeing as high as 3.6 arcsec.

Several special cases may be picked out by examining the component maps in Fig. 8. We highlight J111100 and J130116 (marked with asterisks in Fig. 8). J111100 has two apparent nuclear regions with similar flux requiring three components. This galaxy is discussed in detail in the discussion section, and a full set of maps and spectra are presented in Fig. A6. Throughout the analysis of this galaxy, the two nuclei are not distinguished; therefore plots containing information from the three-component region include both sources. J130116 is a merging pair of galaxies and the AGN is the galaxy in the bottom left of the frame. Complex emission regions are found in both the AGN and its quiescent companion (as evidenced by the two-component regions in the companion). Examination of the spectra shows that this is valid and that there are complex emission line regions in the companion, likely as a result of the merger. When the three-component region of J130116 is discussed, we are referring to the central three-component region of the AGN host, disregarding the scattered three-component spaxels in the companion.

While the maps in Fig. 8 are convincing evidence of complex emission line profiles near the AGN, we cannot conclude that these galaxies possess winds from these alone. We carried out several tests to ascertain whether these multiple components were present due to

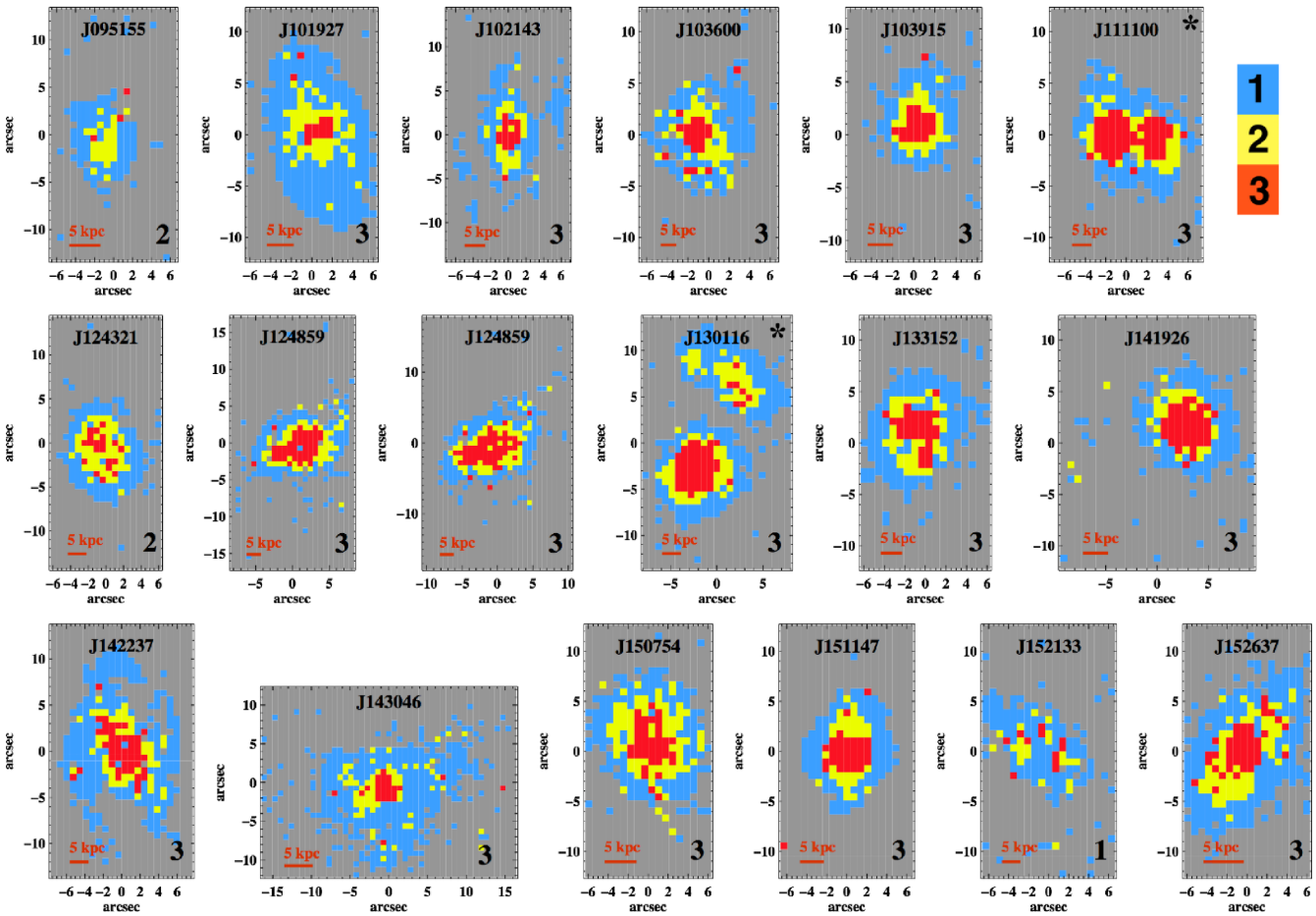


**Figure 8.** Maps showing the preferred number of components in each region of every galaxy in the sample. The number in the bottom-right corner indicates the maximum number of components required (and considered in the analysis) for each galaxy. As the legend on the side states, blue is one-component regions, yellow is two-components, and red is three-components. The grey regions represent data that do not meet the required S/N cut (S/N > 3 in H$\alpha$ and [N II]) and are ignored throughout the analysis. Here, it is clear that the vast majority of galaxies require three components in their central regions near the AGN, and then fewer as we move out into the disc. While this is likely partially S/N dependent, it appears to be primarily driven by line width and complex structure. J111100 and J130116 are marked with asterisks as they will be discussed individually in Section 5.



Downloaded from http://mnras.oxfordjournals.org/ at The Australian National University on July 12, 2016

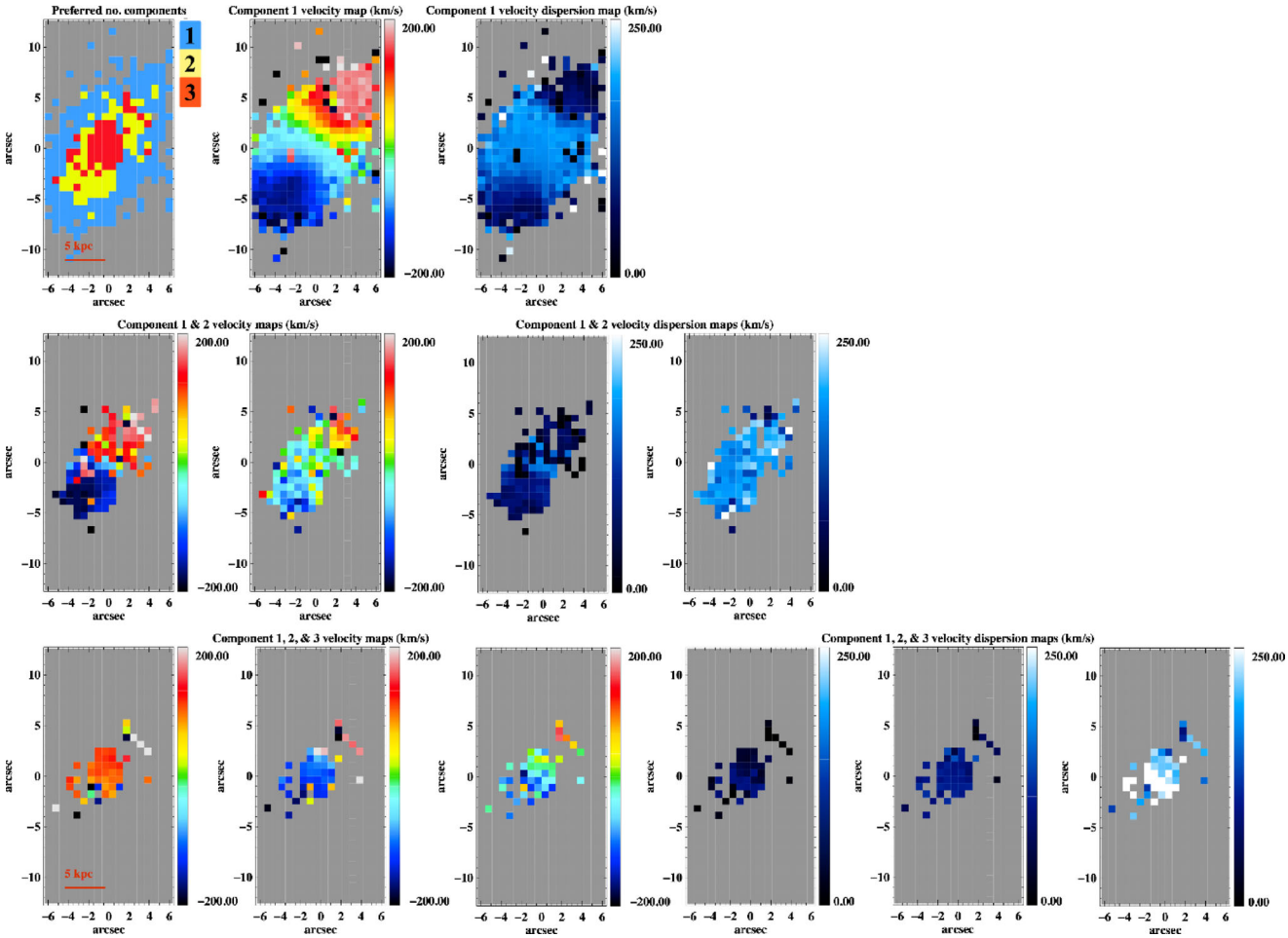


**Figure 9.** Example velocity and velocity dispersion maps for all fitted components of J152637. A map of where each number of components is the preferred model is shown in the top left, with the one-component velocity and velocity dispersion maps next to it. The one-component fits are plotted for data from the entire galaxy to provide a continuous view of the bulk velocity of the galaxy. The second row shows the velocity and velocity dispersion maps of the two-component fits, which are plotted for the two- and three-component regions shown in the component map. Since the components are sorted by dispersion, the velocity map on the left is the narrow component and the one to the right is the broader component. The narrow component shows a velocity discontinuity in the centre due to the rapidly changing flux of the double-peaked emission lines. The broader component appears to follow the overall rotation of the galaxy. The third row shows the velocity and velocity dispersion maps from the three-component fits for only the three-component region. Due to the double-peaked nature of the spectra in the three-component region, we see a narrow redshifted component, a slightly broader blueshifted component, and a broad component with a velocity gradient across the major axis of the galaxy. These components show spatial coherence. We see that each of the components are spatially smooth and show very little noise in the central region.

winds and to conclude whether or not these different components may be rightly considered as separate physical entities.

For multiple components to be considered, they must contribute a significant amount of flux to the fit, and not be only low-level corrections to wings on the emission lines. The narrowest component contributes the least flux to the fit, while components two and three contribute similar levels of flux. Typically, the average contribution from the broad component is 36 per cent across the three-component region, with all falling in the range 17–59 per cent.

### *4.2.1 Coherence of the broad component*

We expect the wind to be most clearly represented by the high-velocity dispersion component that is found. The narrow components may be partly affected by the wind, but the high-velocity dispersion component must be dominated by wind (or BLR, if it is not completely obscured) emission. This means that for galaxies requiring three components, the wind is most dominant in component three, and for galaxies with two components, it is component two. If the broad component is merely accounting for the non-Gaussianity in the emission lines, then we expect the velocity of the broad component to largely trace the velocity of the narrow component, essentially following the bulk rotation of the galaxy. Alternatively, if the velocity of the broad component appears random and noisy showing no structure or coherence, then it likely is not physically meaningful. However, if the velocity is coherent and different from the rotation of the galaxy, then it may represent a real and separate kinematic component of the gas.

To determine whether a component is coherent, we look for spatial smoothness in the velocity and velocity dispersion maps produced by the fitting code. We found all of the broad components appear coherent in both velocity and velocity dispersion, except J102143 which has an extremely broad underlying contribution from the BLR whose extreme broadness ($\sigma$ of up to 1800 km s$^{-1}$) leads to a poorly constrained velocity. The bottom row of Fig. 9

Downloaded from http://mnras.oxfordjournals.org/ at The Australian National University on July 12, 2016

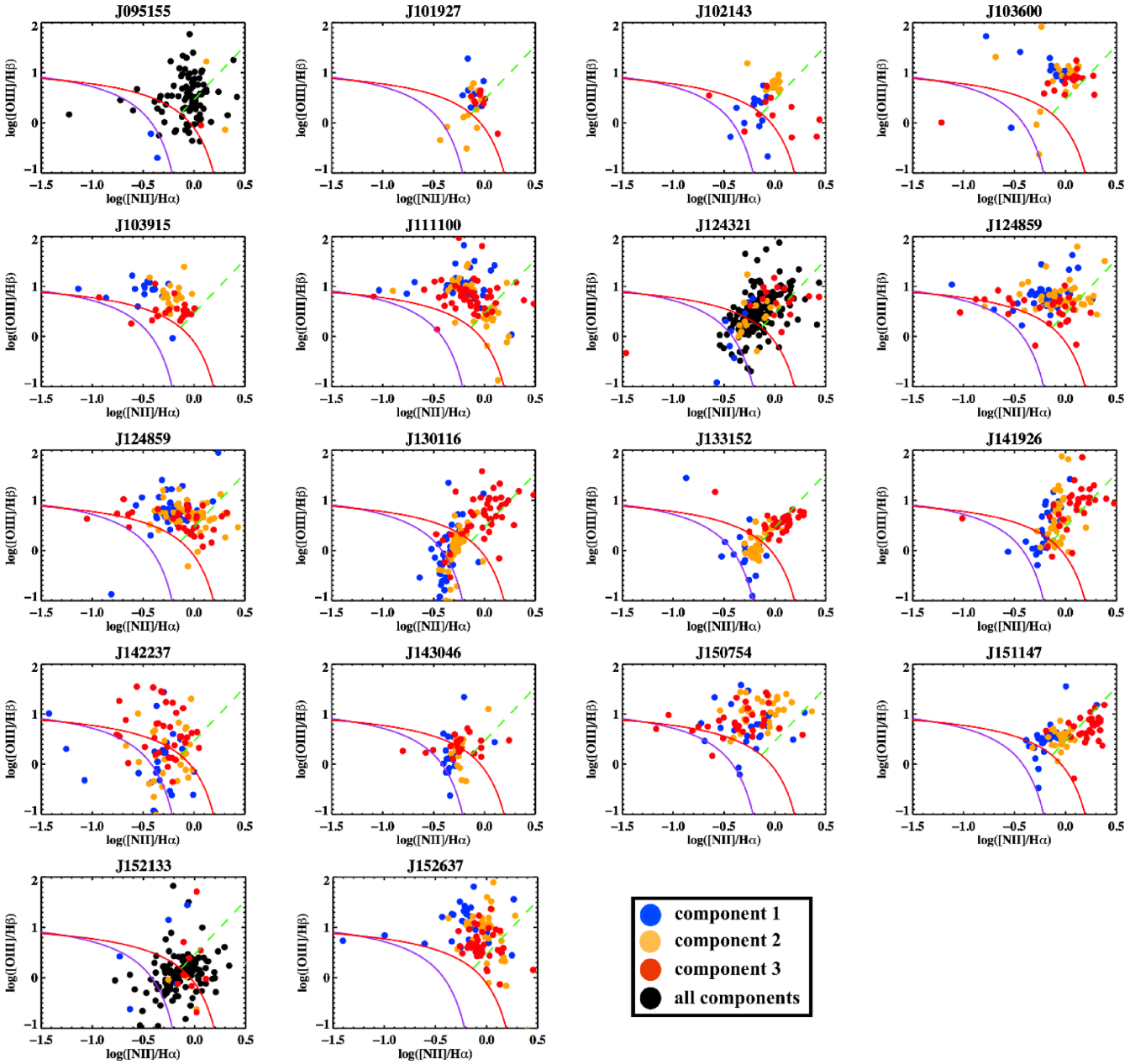


**Figure 10.** BPT diagrams for all galaxies within the sample. As shown in the legend, blue points are the narrowest component, orange are the moderate component, and red are the broad third component. For galaxies without significant resolved three-component regions points from the one- and two-component fits, where each is preferred, are plotted in black in addition to the three-component points where they apply. The purple line is the observed maximum star formation line (Kewley et al. 2001), red is the theoretical star-forming limit (Kauffmann et al. 2003b), and the green line represents the division between Seyferts and LINERs.

shows example maps of velocity and velocity dispersion for the three-component fit to J152637. From these, we see that the velocities and velocity dispersions are spatially smooth.[3]

[3] Since LZIFU sorts component by dispersion rather than tracking them through velocity separation, there are a few spaxels where components one and two switch due to changing dispersion and lead to a discontinuous velocity. This does not generally effect the broad component as it is much broader than components 1 and 2.

### 4.2.2 *Ionization states of the multiple components*

If the wind component (taken to be the third component, which will be most dominated by the wind) is merely random or just the non-Gaussianity of the emission lines, then the ionization state should either be incoherent and noisy, or the same as the rotational component. However, if the ionization is both coherent and different from that of the narrow components, then this is compelling evidence that the broad component traces a kinematically distinct gas component.

To examine the ionization states of the multiple components found in our spectra, we look at two diagnostic plots. The first of these is the typical [N II] BPT diagram (shown in Fig. 10) and the



Downloaded from http://mnras.oxfordjournals.org/ at The Australian National University on July 12, 2016

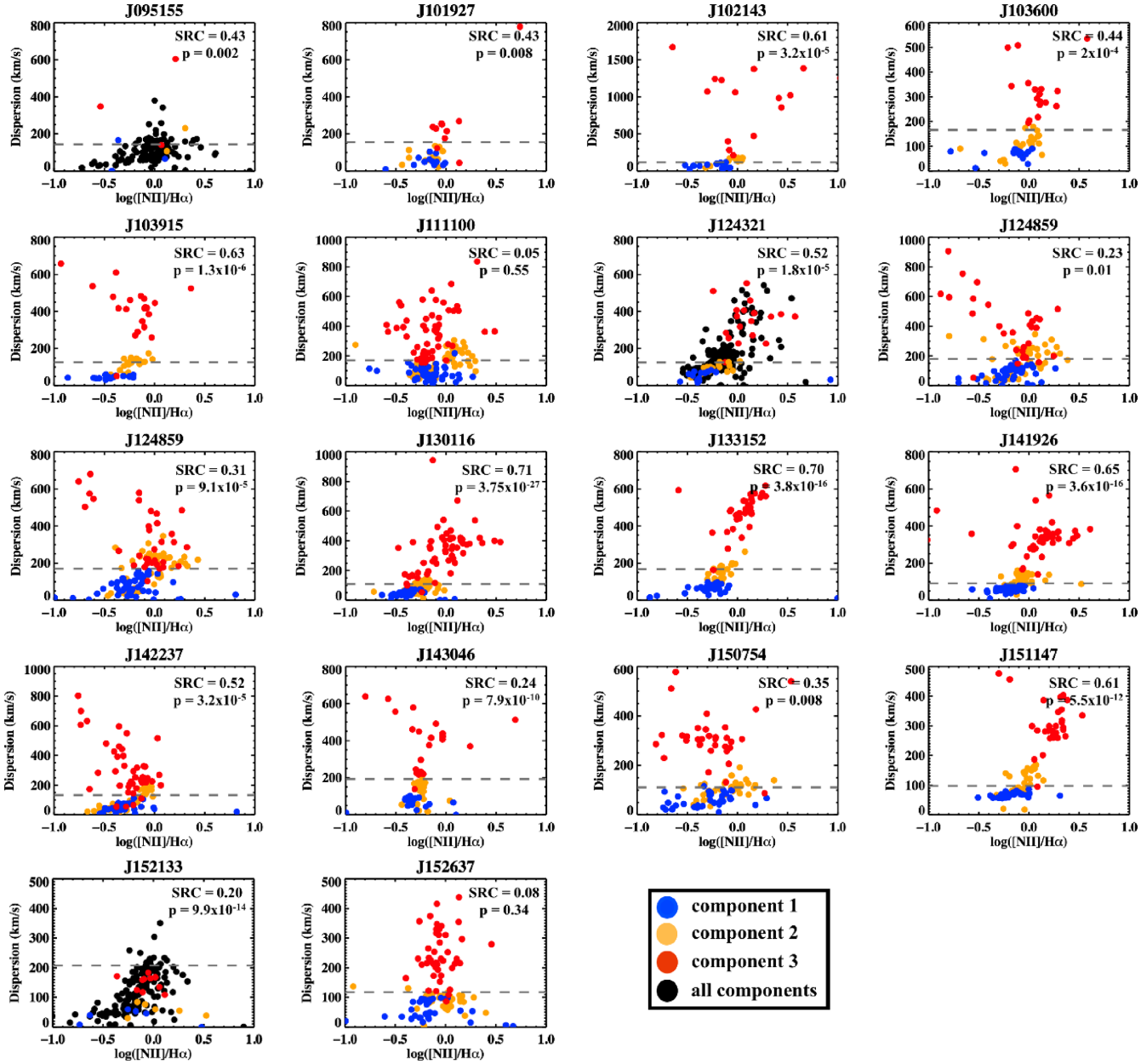


**Figure 11.** Dispersion versus log([N II]/H$\alpha$) for the entire sample. The legend is as in the previous plot, with the narrowest component plotted in blue, the moderate component in orange, the broad component in red, and one- and two-component fits where they are preferred in the three galaxies without significant three-component regions. The horizontal dark grey dashed line shows the median central stellar dispersion. The Spearman rank correlation (SRC) coefficient and corresponding probabilities ($p$) are shown on each plot, the probability corresponding to the probability of the observed correlation in the data occurring by chance. In galaxies where the [N II] emission drops at the highest dispersions, we make a dispersion cut based on where the turn begins prior to calculating the correlation as including this would unnecessarily skew the results. This value was generally around 400 km s$^{-1}$.

second is log([N II]/H$\alpha$) line ratio versus velocity dispersion (shown in Fig. 11). For galaxies with three components only, points from the three-component region are plotted. The blue points represent the narrowest component, the orange is the moderate dispersion component, and the red is the broad component. The three galaxies that did not show significant three-component regions have all their high S/N spaxels plotted in black in Fig. 11 (S/N > 3 in [N II] and H$\alpha$, spaxels where the fits have failed are also removed). The black points are from the one-component fit in the one-component region and the two-component fit in the two-component region. Points from the scattered three-component regions are overplotted in the same way as the other galaxies (as defined by the component maps in Fig. 8). This was done in order to retrieve a reasonable number of points.

Two general trends may be seen in these plots; the first is an increasing line ratio with dispersion which is seen in the vast majority. We used a Spearman's rank correlation coefficient to determine the significance of this trend and found that 15/17 had a probability of <0.05 of the correlation being observed by chance. The exact values are shown in the top-right corner of each panel in Fig. 11 and are listed in Table 2. To calculate the significance of this trend, we only consider points up to a limiting dispersion (typically 400 km s$^{-1}$,

Downloaded from http://mnras.oxfordjournals.org/ at The Australian National University on July 12, 2016

but tuned to each galaxy between 200 and 600 km s$^{-1}$). If the fits tend to lower [N II] emission as dispersion increases, then the limiting dispersion is set to the effective turning point (e.g. for J124859 in Fig. 11, this limit is set to 400 km s$^{-1}$). This is necessary as the behaviour of decreasing [N II] with dispersion is likely due to BLR contribution, and is a separate correlation from the one considered here (though, it is discussed in detail below). The most prominent example of a strong increasing trend of line ratio versus dispersion may be seen in J133152 (third from the left of the third row of Fig. 11). This trend implies that the kinematics and ionization state are coupled, suggesting that they both have the same physical cause. A correlation between these two quantities is often interpreted as strong evidence for shock excitation as photoionization is not known to cause such a trend (see Dopita & Sutherland 1995; Monreal-Ibero, Arribas & Colina 2006; Monreal-Ibero et al. 2010; Rich et al. 2011; Arribas et al. 2014). As the velocity of a shock front increases, so does the excitation and observed line ratio (e.g. Allen et al. 2008). For idealized planar shock fronts, the observed shock velocity and velocity dispersion will not necessarily have similar values. This is because we would only be observing the shock at a single velocity. However, at a sufficiently wide opening angle, the shock velocity and the measured velocity dispersion of the emission can be similar. We would be viewing shock fronts travelling in a range of directions relative to our line of sight, and at different velocities as a result of the inhomogeneous density of the medium. This gives rise to the trend observed between line ratio and dispersion. Ho et al. (2014) show that given this assumption, they are able to exactly reproduce their observed correlation between line ratios and velocity dispersion using shock modelling of their star-forming galaxy. From this, we conclude that we are seeing shock excitation due to an AGN-driven wind. We note that even though the galaxies emission is AGN-like in the central regions, we still see this trend likely resulting from AGN/shock emission mixing. To fully understand what is happening in the future, we will pursue full modelling of these mixing sequences.

Several galaxies show a correlation between line ratio and dispersion coupled with a turn at the higher dispersions back to lower [N II] emission. Extremely broad emission lines with little to no forbidden line flux are suggestive of emission from the BLR, much closer to the SMBH. In order to determine whether this trend is genuine rather than due to low S/N, we inspect the central spectra of the 5/17 galaxies that exhibit this behaviour (J102143 – an example spectrum is shown in Fig. 12, J103915, J124859, J142237, J143046). Of these five, three (J102143, J103915, J124859) show some BLR-like emission in their spectra (very broad emission only present in the Balmer lines). For two galaxies, J142237 and J143046, the fits to the spectra were found to be spatially unstable with some spaxels being fitted with an extremely broad component and some without. This is due to the degeneracies involved in fitting multiple components to these galaxies. It should be noted that these inspections were performed on the entire sample, and others were found to show consistent and stable fits. While we do not claim to be viewing the BLR directly or alone in the remaining three galaxies, as we still see some forbidden line emission from the [N II] lines, it is possible that we are seeing a portion of broad line emission alongside the dominant emission from the NLR in these type II AGN.

#### 4.2.3 What do the components mean?

If component 3 is taken to represent a kinematic component primarily due to the wind, then what are components 1 and 2 representative of? There are several possibilities, they may be due to the disc rotation and therefore be a quiescent star-forming component, or an inflow towards the AGN, or another component of the AGN-driven wind. In this section, we will discuss these possibilities.

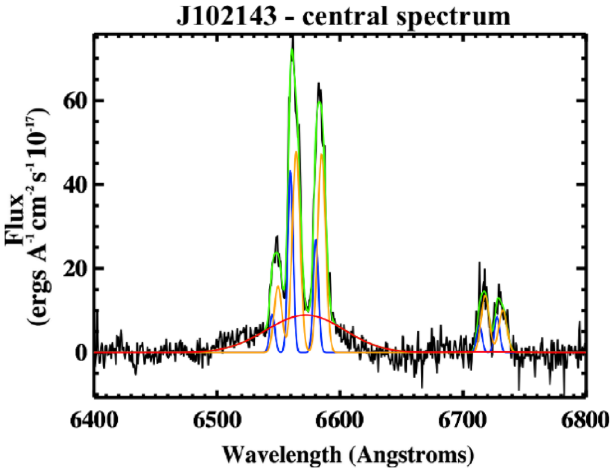


**Figure 12.** A central spectrum for J102143, a galaxy showing a clear negative trend between [N II]/H$\alpha$ and dispersion at the highest dispersions (see Fig. 11). When the spectrum is examined, an underlying broad component in only H$\alpha$ is easily seen. This component has a velocity dispersion > 1000 km s$^{-1}$ and shows no emission in either [N II] or [S II], which supports the theory that it is in fact coming from the BLR.

While we would expect that, were they present, inflows would also be observed as separate offset kinematic components, we do not find evidence for them in our data. There are several reasons for this, most obviously we expect an inflow to be low ionization as it has yet to reach the AGN. We generally do not observe a low-ionization component. Additionally, we would expect an inflow to have low energy, and therefore to have relatively low velocity and velocity dispersion. Even the narrowest components of our fits have velocity dispersion of ≈60 km s$^{-1}$. Finally, the kinematic signatures of inflows are likely only visible very close to the AGN and we are therefore unlikely to be able to resolve them due to our spatial resolution. In order to see signatures of inflows, analysis of the central regions of much lower redshift galaxies would be required (e.g. Riffel et al. 2008).

Rather than an inflow, it is likely that even the narrow components are at least in part due to the outflow. We may gather this from their generally high ionization. Through examination of the BPT diagrams and ionization versus dispersion plots (Figs 11 and 10), we can see that the three components tend to form a continuous trend in both dispersion and ionization. This leads to the conclusion that we have increasing contribution from the outflow. Component 1 has the lowest ionization and dispersion; however, in most galaxies, it still does not fall into the star-forming region of the BPT diagram. Component 2 seems to be a transition component of both moderate dispersion and ionization likely due to increasing contribution to this component from the outflow. Component 3 then represents our wind-dominated component with the highest dispersion and ionization.

In Fig. 9, we show all of the fitted Gaussian components for J152637. In this particular example, we see that the broad components seen in component 2 of the two-component fit (middle row, second from the left) and component 3 of the three-component fit (bottom row, third from the left) are more like the overall rotation of the galaxy than the narrow components. When we examine the

Downloaded from http://mnras.oxfordjournals.org/ at The Australian National University on July 12, 2016

BPT diagram for this source (J152637, Fig. 10), we see that the narrow components have higher [O III] ionization than the broadest component, which tends towards the shock region. From this, we can conclude that none of these components are quiescent and all are due to the AGN and the outflow. This conclusion is supported by the velocities of two narrow components in the three-component region (bottom left of Fig. 9). One of these components is blueshifted and one is redshifted, which suggests that what we are in fact seeing is two sides of a biconical outflow alongside a broad underlying outflowing or shock-related component represented by component 3.

## 5 DISCUSSION

In this paper, we have presented a sample of optically selected, local, luminous type II AGN observed using the AAT's SPIRAL IFU. We have demonstrated that winds are present throughout the sample by analysing the data using non-parametric emission line measures and by considering multiple kinematic components within the spectra. Now, we will discuss the implications of these results and the energies and masses involved.

There are several mechanisms thought to drive winds within galaxies. The primary candidates are star formation and black hole activity. We rule out radio jets as a likely cause due to the radio-quiet nature of the galaxies. Of our 17 sources, 16 are detected in FIRST (Becker, White & Helfand 1995) at 1.4 GHz (see Table 1). In all cases, these are unresolved and the range in radio powers for the detected objects is $1.5 \times 10^{22}$–$4.3 \times 10^{23}$ W Hz$^{-1}$. Most are fainter than the break in the local 1.4 GHz luminosity function at $P_{1.4} \sim 10^{23}$ W Hz$^{-1}$ (Mauch & Sadler 2007) which separates the regions where star-forming galaxies and AGN dominate. This leads us to infer that the kinetic energy from a jet is not driving the outflows we observe. In our multicomponent fits to the central regions of our galaxies, we find that in most cases all components sit in either the AGN or composite part of the BPT diagram (see Fig. 10). Only one galaxy (J130116) shows evidence of a component (the narrowest blue points in Fig. 10) which is dominated by star formation, that is, it lies below the empirical Kauffmann et al. (2003b) line. While it is likely that at least some of our targets also contain ongoing star formation in their central regions, star formation does not dominate the ionizing radiation field in any of them.

Using the central velocity dispersions of our galaxies as measured from the SDSS spectra, we estimate the BH masses in our objects. We use the $M_{\rm BH}$–$\sigma$ relation from Tremaine et al. (2002) of the form

$$\log(M_{\rm BH}/{\rm M}_\odot) = 8.13 + 4.03\log(\sigma/200\,{\rm km\,s^{-1}}). \quad (3)$$

Combining this with the bolometric correction factor for [O III] of 3500 (Heckman et al. 2004), we can estimate the accretion efficiency in our galaxies. The median $L_{\rm Bol}/L_{\rm Edd} = 1.3$ with a range of 0.2–7. There is large uncertainty in this number due to scatter or uncertainties in bolometric corrections, the relationship between galaxy dispersion and $M_{\rm BH}$, and the extinction correction of [O III]; however, within an order of magnitude, we see that our targets must be accreting near the Eddington limit. As a result, it is unsurprising that they are able to drive strong outflows. The winds could be driven directly by radiation pressure from the AGN accretion disc or indirectly through heating or inflating bubbles.

### 5.1 How much energy is in the winds?

In this section, we consider how much energy may be involved in the winds present within the sample. Due to the nature of our data, we are only able to approximate the energy present in the optical emission lines. Since winds and outflows are generally thought to be made up of not only ionized but also molecular and neutral gas (e.g. Rupke & Veilleux 2013), we are calculating what is likely only a small part of the energy involved. In calculating the ionized gas mass, we follow Osterbrock & Ferland (2006). However, thanks to our broader wavelength coverage, encompassing both H$\alpha$ and H$\beta$, we are able to use the luminosity in the H$\alpha$ line and explicitly correct this for extinction using the Balmer decrement. This is somewhat different to other recent authors (e.g. Liu et al. 2013; Harrison et al. 2014) who have used H$\beta$ and have only been able to use population average extinction corrections. The relation we use is

$$\frac{M_{\rm gas}}{0.98\times10^9\,{\rm M}_\odot} = \left(\frac{L_{\rm H\alpha}}{10^{43}\,{\rm erg\,s^{-1}}}\right)\left(\frac{n_{\rm e}}{100\,{\rm cm^{-3}}}\right)^{-1}, \quad (4)$$

where $L_{\rm H\alpha}$ is the extinction corrected H$\alpha$ luminosity. We assume that the entrained gas is confined to the complex emission line regions near the centres of the galaxies, and therefore take the extent of the ionized gas involved in the outflow to be defined by the outer edge of the two-component region (values for this are shown in Table 1). In this calculation, we use the flux measured in all fitted Gaussian components. We do this because all of the components generally have high ionization and as a result are likely, at least partially, associated with the outflow.

We calculate the electron density, $n_{\rm e}$, based on the measured ratio of the [S II] emission doublet. We find an average ratio of 1.3 (typically varying between 1 and 1.7) that gives an $n_{\rm e} \approx 100{\rm cm}^{-3}$ according to the relation provided by Osterbrock & Ferland (2006), which is consistent with other results (Greene et al. 2011). Using this, we find an ionized gas mass, $M_{\rm gas} = (1-20)\times10^9$ M$_\odot$ , with a median of $6 \times 10^9$ M$_\odot$ . This value for gas mass may then be converted to an energy simply using

$$E_{\rm kin} = \frac{1}{2}\,M_{\rm gas}\,v_{\rm gas}^2. \quad (5)$$

We take that the gas velocity is taken to be $W_{80}$/1.3 as done by Harrison et al. (2014) and Liu et al. (2013) to approximate outflow velocities of wide opening angle bi-conical outflow models.[4] From this, we find $E_{\rm kin} = (1$–$36) \times 10^{57}$ erg, with a median of $7 \times 10^{57}$ erg. This value is slightly higher than what Harrison et al. (2014) find, likely since they do not correct for extinction. This is supported by the fact that Liu et al. (2013) find a very similar number using an average extinction correction.

Using the extent of the ionized gas regions within the sample and the gas velocity used above ($W_{80}$/1.3), we may then use $v_{\rm out} = D_{\rm em}/2t_{\rm out}$ to determine a time-scale for the outflow (where $D_{\rm em}$ is the diameter of the region containing gas ionized by the AGN). This leads to a value of $t_{\rm out} \approx 6$ Myr, allowing for a time-averaged wind power (in ionized gas) to be calculated, resulting in $\dot{E}_{\rm out} \approx (5-190) \times 10^{42}$ erg s$^{-1}$. If we then calculate the median ratio of wind power to bolometric luminosity, we find it to be ~0.02 per cent. This demonstrates that the AGN is easily able to drive the outflows, even accounting for the extra mass in neutral atomic or molecular gas not seen in our study.

To calculate an order of magnitude mass outflow rate, we assume that the outflows are spherically symmetric. Following Rodríguez Zaurín et al. (2013) and Harrison et al. (2014), and assuming that our outflow velocity is approximately equal to $W_{80}$/1.3 (we do not use

[4] Note that use of the traditional $E = \frac{1}{2}M(v^2 + \sigma^2)$ yields results of the same order of magnitude, but we do not use this due to the dependence of velocity on orientation which leads to a wide variety of observed velocities.

Downloaded from http://mnras.oxfordjournals.org/ at The Australian National University on July 12, 2016

$\Delta v$ here due to the uncertainty in what this quantity truly represents in our sample and the unknown degree to which it is effected by beam smearing), we find outflow rates, $M_{\rm out} \approx 370$–$2700\,{\rm M}_{\odot}\,{\rm yr}^{-1}$. These values are well below the upper limit of $1.9 \times 10^4\,{\rm M}_{\odot}\,{\rm yr}^{-1}$ derived by Liu et al. (2013). Our derived outflow rates are dramatically larger than outflow rates typical of the nearest low-luminosity AGN, which are generally of the order of $1.0\,{\rm M}_{\odot}\,{\rm yr}^{-1}$ (e.g. Storchi-Bergmann et al. 2010; Riffel, Storchi-Bergmann & Winge 2013); this difference is likely due to the much greater luminosity of our sample.

### 5.2 Outflows and shocks

We showed in Section 4.2.2 that most of the sample have a significant correlation between dispersion and excitation. This trend is generally taken to indicate the presence of shocks, as it is evident that in shocked gas, excitation must be linked to the velocity of the shock front (Dopita & Sutherland 1995). Further, in wide-angle outflows, a range of velocities will be observed due to a range of outflow directions compared to our line of sight. As a result, we expect the measured line widths to correlate well with the typical shock velocities in the outflows (i.e. we always see some gas with its velocity parallel to our line of sight). Therefore, the natural explanation for the observed correlation between excitation and dispersion is the presence of shocks in the gas. It is worth noting that we see correlations between line dispersion and ionization even when most or all of the spaxels in a galaxy are above both the LINER and theoretical maximal star formation line in the BPT diagram. We therefore expect the ionization in these objects to be due to a mix of photoionization from the AGN and shock ionization.

Having seen high velocities indicative of outflows, it should not be surprising that we find evidence of shocks in the surrounding gas, as a high-velocity outflow propagating through a medium is expected to cause shocks. Evidence supporting this has been found in several different kinds of galaxy such as luminous infrared galaxies (Monreal-Ibero et al. 2006; Monreal-Ibero et al. 2010), mergers (Rich et al. 2011), and star-forming galaxies (Ho et al. 2014).

We finally note that our selection method potentially biases against the most shock-dominated AGN, as we exclude objects with central (SDSS) spectra that indicate that they lie below the LINER/Seyfert divide in the BPT diagram. That said, we note that above $\log[L_{[{\rm O\,III}]}/{\rm L}_{\odot}] = 8.7$, only $\simeq 20$ per cent of objects lie below this line.

### 5.3 J111100

The galaxy J111100 shows a prominent double peak in its emission line flux. The galaxy appears morphologically disturbed with tidal features and is a possible merger remnant. The distribution of the H$\alpha$ flux compared to the continuum light from the blue data is shown in Fig. 13 (top right). The H$\alpha$ flux peak on the left-hand side aligns well with the continuum (contours) suggestive of a typical centrally located AGN. The H$\alpha$ flux peak on the right-hand side has no significant continuum peak associated with it. When we examine the galaxy's kinematics, we find that the stars are rotating regularly, but that the gas shows no large-scale rotation and has several discontinuities (see Fig. A6).

An average spectrum from a $3 \times 3$ spaxel bin is plotted in Fig. 13 centred on the two H$\alpha$ flux peaks. The central spectrum is very broad with blended emission lines; this is indicative of an outflow driven by the central AGN or potentially a contribution from the BLR. The second source, however, shows much narrower emission

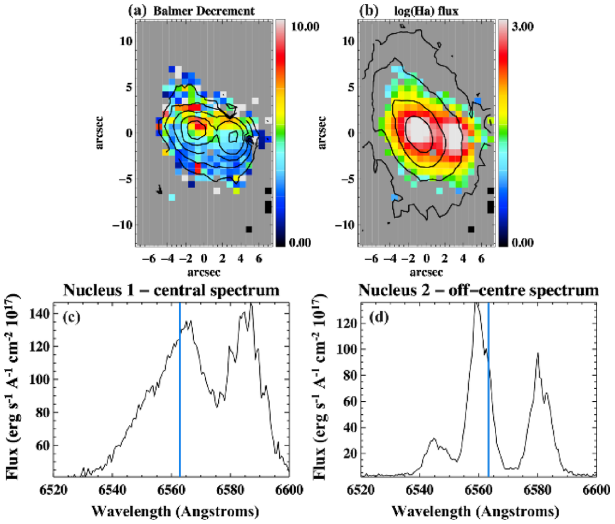


**Figure 13.** (a) Balmer decrement map for J1111000 with contours spaced by 1 mag intervals of H$\alpha$ flux overlaid. (b) H$\alpha$ flux map in $10^{17}$erg s$^{-1}$ Å$^{-1}$ cm$^{-2}$ with stellar continuum contours from the blue data overlaid. (c)–(d) Spectrum of central emission line peak. Bottom right: spectrum of offset emission line peak. For both spectra, the vertical line shows the location of H$\alpha$ at rest.

lines (though the dispersion is still $\approx 200\,{\rm km\,s}^{-1}$). When we look at the relative fluxes of the two sources, we find that the off-centre source is in fact brighter (observed H$\alpha$ flux) than the central source by $\approx 20$ per cent. This is somewhat surprising, but can be explained by the greater extinction see towards the line of sight of the central source (see the Balmer decrement map in Fig. 13).

There are several possible explanations for the structure in this source, which we discuss in turn. Given that both peaks show line ratios consistent with AGN ionization, we could argue that we are seeing two separate AGN (i.e. two accreting black holes). However, the lack of any significant continuum associated with the offset emission line source means that this is unlikely unless one black hole is ejected from its host during the merger process. While we cannot rule out such an ejection hypothesis, the narrow-emission-line gas we see will not in general be gravitationally bound to the black hole, so an ejected black hole would likely have had to be ejected in the direction of a sufficiently large gas cloud that it could then ionize. Alternatively, we are seeing ionization from a single black hole. In this case, the morphology we are seeing may be driven by other characteristics of the galaxy. For example, could a dust lane cause the two peak nature of this source? We find this to be unlikely as a map of Balmer decrements (Fig. 13) does not show an excess between the two peaks. We are thus left with the hypothesis that the offset emission line flux is due to gas ionized by the central AGN. The surprising feature here is the high luminosity of the offset emission-line peak at a distance of at least 6 kpc (projected) from the nucleus. The central AGN has a log(H$\alpha$) luminosity of 42.76 erg s$^{-1}$ before extinction correction and 43.53 erg s$^{-1}$ after correction for extinction. The off-centre source has a similar luminosity prior to extinction correction, log(H$\alpha$) of 42.6 erg s$^{-1}$, and due to the lower extinction at the location of this source, this becomes 42.99 erg s$^{-1}$ after correction. This object is discussed in Keel et al. (2012) as a part of a search for AGN that show emission line clouds similar to the Hanny's Voorwerp discovered by the Galaxy Zoo project. This luminosity ratio between the central AGN and the cloud is very similar to the objects in the Keel et al. survey that has sufficient data for these calculations. For J111100, they are not able to resolve the



Downloaded from http://mnras.oxfordjournals.org/ at The Australian National University on July 12, 2016

cloud and suggest that follow-up spectroscopy will be required to decipher what is going on in this system. An ionized gas cloud is the most plausible explanation, but we will discuss this galaxy further in a separate paper, including additional data to further diagnose its physical nature.

## 6 CONCLUSIONS

In this paper, we have presented a kinematic analysis of 17 local, luminous, type II AGN observed with the SPIRAL IFU on the AAT. By selecting this sample, our aim was to determine how widespread winds and outflows are in luminous AGN through analysis of the detailed information provided by spatially resolved spectroscopy. Through analysis of the kinematics, we determined that winds were detected in some form in the entire sample. Here, we present a summary of our conclusions.

(i) We find complex emission features suggestive of winds in 100 per cent of the sample, while 16/17 galaxies (and all those with high S/N) show strong evidence for significant multiple velocity components in their spectra.

(ii) Of the galaxies that possess multiple components, all have properties that suggest that they have a wind component, high dispersion, and high excitation.

(iii) Examination of the ionization states of our multiple components showed a correlation between the kinematics and the line ratio in 15/17 of the galaxies, implying that both are being driven by the same source. The majority (12/17) showed a positive trend, indicating the presence of shocks. A further three galaxies show this trend alongside a turn back to lower [N II] emission at the highest dispersions which is evidence for a contribution from BLR emission (which was confirmed through examination of their spectra).

In future work, we will aim to more fully characterize the outflows in these galaxies by combining dynamical models of the stellar kinematics with modelling of the outflows, including the contribution from shocks. Galaxies from the SAMI Galaxy Survey (see Croom et al. 2012) will also be used as a control sample to see how AGN feedback varies with AGN power by selecting lower luminosity AGN.

## ACKNOWLEDGEMENTS

We thank the anonymous referee for their helpful comments which improved the clarity of the paper. This research was based on data taken with the Anglo-Australian Telescope. Parts of this research were conducted by the Australian Research Council Centre of Excellence for All-sky Astrophysics (CAASTRO) through project number CE110001020. SMC acknowledges the support of an ARC future fellowship (FT100100457).

## REFERENCES

Abazajian K. N. et al., 2009, ApJS, 182, 543
Allard F., Hauschildt P. H., Alexander D. R., Tamanai A., Schweitzer A., 2001, ApJ, 556, 357
Allen M. G., Groves B. A., Dopita M. A., Sutherland R. S., Kewley L. J., 2008, ApJS, 178, 20
Allen J. T. et al., 2014, MNRAS, in press
Antonucci R., 1993, ARA&A, 31, 473
Arribas S., Colina L., Bellocchi E., Maiolino R., Villar-Martín M., 2014, A&A, 568, A14
Baldwin J. A., Phillips M. M., Terlevich R., 1981, PASP, 93, 5
Barrows R. S., Sandberg Lacy C. H., Kennefick J., Comerford J. M., Kennefick D., Berrier J. C., 2013, ApJ, 769, 95
Becker R. H., White R. L., Helfand D. J., 1995, ApJ, 450, 559
Bower R. G., Benson A. J., Malbon R., Helly J. C., Frenk C. S., Baugh C. M., Cole S., Lacey C. G., 2006, MNRAS, 370, 645
Bryant J. J. et al., 2014, MNRAS, in press
Cappellari M., Emsellem E., 2004, PASP, 116, 138
Comerford J. M., Schluns K., Greene J. E., Cool R. J., 2013, ApJ, 777, 64
Cowie L. L., Songaila A., Kim T.-S., Hu E. M., 1995, AJ, 109, 1522
Croom S. M. et al., 2012, MNRAS, 421, 872
Croton D. J. et al., 2006, MNRAS, 365, 11
Dopita M. A., Sutherland R. S., 1995, ApJ, 455, 468
Fischer T. C., Crenshaw D. M., Kraemer S. B., Schmitt H. R., Mushotsky R. F., Dunn J. P., 2011, ApJ, 727, 71
Ganguly R., Brotherton M. S., 2008, ApJ, 672, 102
González Delgado R. M., Cerviño M., Martins L. P., Leitherer C., Hauschildt P. H., 2005, MNRAS, 357, 945
Gray R. O., Corbally C. J., 1994, AJ, 107, 742
Greene J. E., Zakamska N. L., Ho L. C., Barth A. J., 2011, ApJ, 732, 9
Harrison C. M. et al., 2012, MNRAS, 426, 1073
Harrison C. M., Alexander D. M., Mullaney J. R., Swinbank A. M., 2014, MNRAS, 441, 3306
Hauschildt P. H., Baron E., 1999, J. Comput. Appl. Math., 109, 41
Heckman T. M., Miley G. K., van Breugel W. J. M., Butcher H. R., 1981, ApJ, 247, 403
Heckman T. M., Kauffmann G., Brinchmann J., Charlot S., Tremonti C., White S. D. M., 2004, ApJ, 613, 109
Ho I.-T. et al., 2014, MNRAS, 444, 3894
Hönig S. F. et al., 2013, ApJ, 771, 87
Hopkins P. F., Hernquist L., Cox T. J., Di Matteo T., Robertson B., Springel V., 2006, ApJS, 163, 1
Kauffmann G. et al., 2003a, MNRAS, 341, 33
Kauffmann G. et al., 2003b, MNRAS, 346, 1055
Keel W. C. et al., 2012, MNRAS, 420, 878
Kewley L. J., Dopita M. A., Sutherland R. S., Heisler C. A., Trevena J., 2001, ApJ, 556, 121
Lanz T., Hubeny I., 2003, ApJS, 146, 417
Liu G., Zakamska N. L., Greene J. E., Nesvadba N. P. H., Liu X., 2013, MNRAS, 436, 2576
Martins L. P., González Delgado R. M., Leitherer C., Cerviño M., Hauschildt P., 2005, MNRAS, 358, 49
Mauch T., Sadler E. M., 2007, MNRAS, 375, 931
Monreal-Ibero A., Arribas S., Colina L., 2006, ApJ, 637, 138
Monreal-Ibero A., Arribas S., Colina L., Rodríguez-Zaurín J., Alonso-Herrero A., García-Marín M., 2010, A&A, 517, A28
Mullaney J. R., Alexander D. M., Fine S., Goulding A. D., Harrison C. M., Hickox R. C., 2013, MNRAS, 433, 622
Murray N., Quataert E., Thompson T. A., 2005, ApJ, 569
Nenkova M., Sirocky M. M., Nikutta R., Ivezić Ž., Elitzur M., 2008, ApJ, 685, 160
Osterbrock D. E., Ferland G. J., 2006, Astrophysics of Gaseous Nebulae and Active Galactic Nuclei. University Science Books, Mill Valley, CA
Reyes R. et al., 2008, AJ, 136, 2373
Rich J. A., Kewley L. J., Dopita M. A., 2011, ApJ, 734, 87
Riffel R. A., Storchi-Bergmann T., Winge C., McGregor P. J., Beck T., Schmitt H., 2008, MNRAS, 385, 1129
Riffel R. A., Storchi-Bergmann T., Winge C., 2013, MNRAS, 430, 2249
Riffel R. A., Storchi-Bergmann T., Riffel R., 2014, ApJ, 780, L24
Rodríguez Zaurín J., Tadhunter C. N., Rose M., Holt J., 2013, MNRAS, 432, 138
Rupke D. S. N., Veilleux S., 2013, ApJ, 768, 75
Saunders W. et al., 2004, in Moorwood A. F. M., Iye M., eds, Proc. SPIE Conf. Ser. Vol. 5492, Ground-based Instrumentation for Astronomy. SPIE, Bellingham, p. 389
Scannapieco E., Oh S. P., 2004, ApJ, 608, 62
Sharp R., Birchall M. N., 2010, PASA, 27, 91
Sharp R. G., Bland-Hawthorn J., 2010, ApJ, 711, 818

Downloaded from http://mnras.oxfordjournals.org/ at The Australian National University on July 12, 2016

Sharp R. et al., 2006, in McLean I. S., Iye M., eds, Proc. SPIE Conf. Ser. Vol. 6269, Ground-based and Airborne Instrumentation for Astronomy. SPIE, Bellingham, p. 62690G
Sharp R. et al., 2014, MNRAS, in press
Storchi-Bergmann T., Lopes R. D. S., McGregor P. J., Riffel R. A., Beck T., Martini P., 2010, MNRAS, 402, 819
Tremaine S. et al., 2002, ApJ, 574, 740
Vega Beltrán J. C., Pizzella A., Corsini E. M., Funes J. G., Zeilinger W. W., Beckman J. E., Bertola F., 2001, A&A, 374, 394
Veilleux S., Osterbrock D. E., 1987, ApJS, 63, 295
Veilleux S. et al., 2013, ApJ, 776, 27
Villar-Martín M., Humphrey a., Delgado R. G., Colina L., Arribas S., 2011, MNRAS, 418, 2032
Whittle M., 1985, MNRAS, 213, 1

## APPENDIX A: GALAXY BY GALAXY FIGURES

In this Appendix, a standard set of figures is presented for each galaxy, and all have the same format as is described in Fig. A1. A sample of this appendix is presented in this paper, the rest of the appendix is available in the online version.

## SUPPORTING INFORMATION

Additional Supporting Information may be found in the online version of this article:

**Appendix A: Galaxy by galaxy Figs** (http://mnras.oxfordjournals.org/lookup/suppl/doi:10.1093/mnras/stu2224/-/DC1).
Please note: Oxford University Press is not responsible for the content or functionality of any supporting materials supplied by the authors. Any queries (other than missing material) should be directed to the corresponding author for the paper.

This paper has been typeset from a TEX/LATEX file prepared by the author.

Downloaded from http://mnras.oxfordjournals.org/ at The Australian National University on July 12, 2016